Modeling of radiation and nitric oxide formation in turbulent nonpremixed flames using a flamelet/progress variable formulation

Matthias Ihme and Heinz Pitsch

Additional information on Phys. Fluids

Modeling of radiation and nitric oxide formation in turbulent nonpremixed flames using a flamelet/progress variable formulation

Matthias Ihme[a)] and Heinz Pitsch

Department of Mechanical Engineering, Building 500, Stanford University, Stanford, California 94305, USA

A model for the prediction of the nitric oxide (NO) formation in turbulent nonpremixed flames is proposed. Since the NO formation has a strong temperature sensitivity, the accurate prediction of the flame temperature under the consideration of radiative heat losses is required. The first part of the paper addresses the extension of a flamelet-based combustion model to account for radiative heat loss effects by introducing enthalpy as an additional parameter. A transport equation for enthalpy is solved, and the radiative sink term in this equation is obtained from unsteady flamelet solutions. The model is applied to a large-eddy simulation (LES) of Sandia flame D, and the importance of the interaction between turbulence and radiation on temperature and mixture fraction is investigated. Based on the radiative flamelet formulation, a consistent model for the prediction of NO formation is developed in the second part of the paper. In this model, an additional transport equation for the NO mass fraction is solved, and the chemical source term is obtained from a flamelet library. Since the consumption rate is dependent on the NO mass fraction, this term requires modeling, which is discussed in this paper. By employing a scale similarity argument, a closure model for application in LES is presented. After the analysis of the proposed model for the thermal, nitrous oxide, and prompt pathways for NO formation, the NO model is integrated into the extended flamelet/progress variable model and applied in LES of Sandia flame D and a Pratt & Whitney aircraft engine combustor configuration. © *2008 American Institute of Physics*. [DOI: 10.1063/1.2911047]

I. INTRODUCTION

The emission of carbon dioxide (CO_2) and pollutants, such as unburned hydrocarbons (UHCs), carbon monoxide (CO), and oxides of nitrogen (NO_x), from combustion processes has gained increasing attention over the past few decades. While CO_2 is considered to be a major greenhouse gas, NO_x is regarded as precursor of chemical smog and as contributor to stratospheric ozone depletion.[1] Devising technologies which reduce emissions of such critical species into the atmosphere requires the understanding and control of their formation mechanisms.

Nitric oxide (NO) and nitrogen dioxide (NO_2), collectively referred to as NO_x, are typically formed on time scales which are slow compared to fuel oxidation reactions. This slow formation process, together with the short residence times in modern combustion devices, implies that NO_x is usually emitted at concentrations substantially below equilibrium values.[2] The slow formation and its strong dependence on the flame temperature represent major difficulties for the accurate prediction of NO_x. An example of the strong temperature dependence is shown in Fig. 1. The left panel of this figure shows the steady-state NO mole fraction $X_{NO,st}$, as a function of the scalar dissipation rate at stoichiometric mixture fraction $\chi_{Z,st}$ for a methane/air flame at standard condition. $X_{NO,st}$ as a function of the corresponding stoichiometric temperature Θ_{st} is shown in the right panel of Fig. 1. This figure illustrates the temperature sensitivity of NO, suggesting that the accurate modeling of the temperature by accounting for radiation and wall heat losses is of paramount importance for its prediction.

Several models have been proposed for the prediction of nonpremixed turbulent combustion processes in both Reynolds-averaged Navier–Stokes (RANS) simulations and large-eddy simulations (LESs). Among these are the flamelet models,[3,4] the transported probability density function (TPDF) method,[5,6] the conditional moment closure (CMC) method,[7] and the linear eddy model.[8] In many applications of combustion LES, steady laminar flamelet models (SLFMs) have been applied not only in simulations of jet flames[9–11] but also to more complex flows such as gas turbine combustors.[12–14]

The SLFM can be derived from the unsteady flamelet equations, which are obtained through a coordinate transformation of the transport equations for species and temperature by introducing the mixture fraction Z as an independent coordinate.[15] The unsteady flamelet equations can be written as

$$\partial_t \boldsymbol{\phi} - \frac{\chi_Z}{2} \partial_Z^2 \boldsymbol{\phi} = \dot{\boldsymbol{\omega}}, \tag{1}$$

where $\dot{\boldsymbol{\omega}}$ is the source term of all species and temperature, denoted by $\boldsymbol{\phi}$, and $\chi_Z = 2\alpha|\nabla Z|^2$ is the scalar dissipation rate with α denoting the molecular diffusivity. Note that the source term in the temperature equation also contains terms describing the enthalpy flux by mass diffusion and, possibly, also a radiative source term.

[a)]Present address: Department of Aerospace Engineering, University of Michigan, Ann Arbor, MI 48109. Author to whom correspondence should be addressed. Electronic mail: mihme@umich.edu.
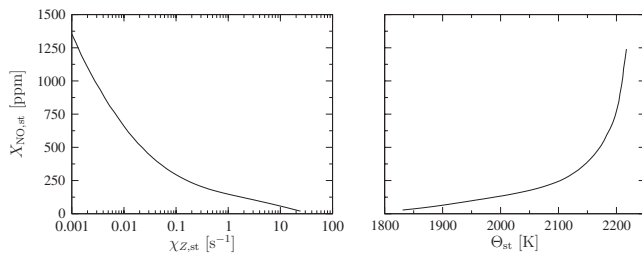
FIG. 1. NO mole fraction as a function of scalar dissipation rate at stoichiometry for a methane/air flame at standard condition (left) and corresponding dependence of $X_{NO,st}$ on temperature (right).

Under the assumption that all species are formed on a sufficiently fast time scale, the temporal derivative in Eq. (1) can be neglected. This results in the steady laminar flamelet equations, which can be written as

$$-\frac{\chi_Z}{2}\partial_Z^2\boldsymbol{\phi} = \dot{\boldsymbol{\omega}}, \tag{2}$$

and all thermochemical quantities are a function of mixture fraction and scalar dissipation rate only. The solution of these equations can be represented by the so-called S-shaped curve, which is shown in Fig. 2(a). The solid lines in this figure correspond to the solution of the steady flamelet equations without radiative heat losses. The upper and lower branches of this curve describe the stable burning and non-burning steady states, while the middle branch is unstable. The turning point between the upper and middle branches is denoted by $\chi_{Z,q}$, corresponding to the critical scalar dissipation rate at which quenching occurs.

All thermochemical quantities, which are denoted by the vector $\boldsymbol{\psi}$, along this curve can then be written in the form

$$\boldsymbol{\psi} = \mathcal{E}_{\boldsymbol{\psi}}(Z, \chi_Z), \tag{3}$$

and $\mathcal{E}_{\boldsymbol{\psi}}$ refers to the steady laminar flamelet library. Note, however, that this vertical projection onto the $\chi_Z - Z$ plane is not unique and results in multiple solutions when $\chi_{Z,st} \leq \chi_{Z,q}$. An example is given in Fig. 2(b), showing four different temperature profiles, which are computed with the
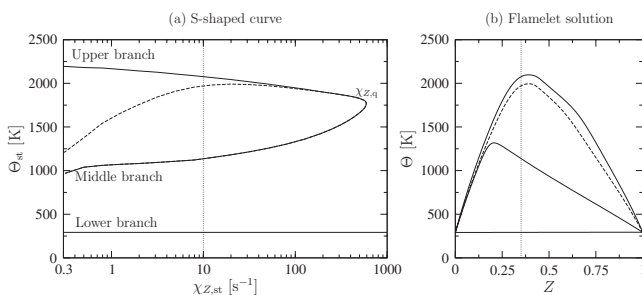

FIG. 2. Solutions of the flamelet equations for a partially premixed methane-air flame, showing (a) temperature as a function of the scalar dissipation rate at stoichiometric mixture fraction $Z_{st} = 0.351$. The solid lines show the solution of the steady flamelet equations without radiative heat losses, consisting of the stable lower and upper branches and the unstable middle branch. The steady flamelet solution under consideration of radiative effects is shown by the dashed line. (b) Steady temperature profiles of four flamelets, computed for the same scalar dissipation rate $\chi_{Z,st} = 10$ s^{-1}, and the vertical dashed line shows the location of the stoichiometric mixture.

same scalar dissipation rate of $\chi_{Z,st} = 10$ s^{-1}. These flamelets can be identified by the intersections of the vertical dotted line with the solution curve of the steady flamelet equations in Fig. 2(a). In order to overcome the ambiguity of the steady flamelet model, a reaction progress parameter Λ has been introduced in the flamelet/progress variable (FPV) model.[16,17] This parameter is chosen so that it uniquely identifies each single flame state along the S-shaped curve, including the unstable branch. The definition of Λ makes use of a reaction progress variable C, which can itself be represented, for instance, by the temperature or by a linear combination of major reaction product mass fractions.[17] In the following, the reaction progress variable is defined as $C = Y_{CO_2} + Y_{CO} + Y_{H_2O} + Y_{H_2}$ and Y_i denotes the mass fraction of species i. A possible definition of the reaction progress parameter could be

$$\Lambda = C|Z_{st}, \tag{4}$$

corresponding to the value of the progress variable of each flamelet, evaluated at the stoichiometric condition. With this, the flamelet library in the FPV model can be written as

$$\boldsymbol{\psi} = \mathcal{F}_{\boldsymbol{\psi}}(Z, \Lambda), \tag{5}$$

and $\mathcal{F}_{\boldsymbol{\psi}}$ denotes the FPV library. Note that this is different from Eq. (3), as it includes all solutions of the adiabatic steady-state flamelet equations. The reaction progress variable C can then be expressed as

$$C = \mathcal{F}_C(Z, \Lambda). \tag{6}$$

In principle, an equation for Λ can be solved;[18] however, such a solution requires modeling of cross-dissipation terms for application in turbulent reacting flows, which is nontrivial. Instead, it appears to be more convenient to directly solve a transport equation for C and parametrize the flamelet table in terms of Z and C. In the FPV model, this is done as follows. Under the assumption that $\mathcal{F}_C$ is bijective, Λ can be expressed in terms of Z and C:

$$\Lambda = \mathcal{F}_C^{-1}(Z, C). \tag{7}$$

Eliminating Λ by inserting this expression into Eq. (5) allows all thermochemical quantities to be expressed in terms of the mixture fraction and progress variable only. With this, the state relation can be written as

$$\boldsymbol{\psi} = \mathcal{G}_{\boldsymbol{\psi}}(Z, C), \tag{8}$$

with $\mathcal{G}_{\boldsymbol{\psi}}(Z, C) = \mathcal{F}_{\boldsymbol{\psi}}(Z, \mathcal{F}_C^{-1}(Z, C))$. The FPV model requires then the solution of the following transport equations for Z and C:

$$\rho\mathcal{D}_t Z = \nabla \cdot (\rho\alpha\nabla Z), \tag{9a}$$

$$\rho\mathcal{D}_t C = \nabla \cdot (\rho\alpha\nabla C) + \rho\dot{\omega}_C, \tag{9b}$$

where ρ is the density, $\dot{\omega}_C$ is the chemical source term of the progress variable, and $\mathcal{D}_t = \partial_t + \boldsymbol{u}\cdot\nabla$ is the substantial derivative.

It is important to note that models that are based on the steady laminar flamelet equations assume that the chemical state of a particular flamelet relaxes to the steady-state solu-

tion on a sufficiently fast time scale, justifying that the unsteady term in Eq. (1) can be neglected. Therefore, slow processes such as radiation or NO formation cannot be predicted with such models.[19] Unsteady flamelet models, on the other hand, are able to account for different chemical time scales. However, these models introduce a Lagrangian time scale information, which restricts their application to rather simple flow configurations.

Despite the aforementioned limitations of the SLFM, extensions have been proposed which incorporate radiative effects into this model.[20–22] In these models, coupling between radiation and chemistry is achieved by introducing the enthalpy defect as an additional reaction coordinate. Steady laminar flamelets are hereby generated by reducing the temperature at the boundaries to achieve the required enthalpy defects. A major shortcoming of this procedure is that it leads to unrealistic low temperatures at the boundaries for large enthalpy defects. This is remedied by either reducing the solution domain in mixture fraction space[21] or changing the mixture composition at the boundaries.[22] Furthermore, the somewhat arbitrary specification of a uniform enthalpy defect across a laminar flamelet may result in an unphysical description of the corresponding flame structure. Nevertheless, it was demonstrated in different applications that these models lead to improved temperature predictions; however, it is believed that the relative slow NO formation is not accurately captured since steady laminar flamelets are employed.

The objective of this paper is the development of a model for the prediction of NO formation by employing the FPV approach. Because the formation of NO has a strong temperature sensitivity, an extension of the FPV model is presented in Sec. II, which is able to account for radiative heat loss effects. In this model, enthalpy H is introduced as an additional variable, and heat loss effects in the optically thin limit are considered by solving an additional transport equation for H.

Based on this extended FPV formulation, a model for the prediction of the NO formation is presented in Sec. III. The accuracy of the model is assessed for the three major NO formation pathways and is compared to unsteady flamelet results in Sec III B. Following this analysis, the model is formulated for application in LES and numerical simulations of two different flow configurations are performed in Sec. IV. In the first application, Sandia flame D is computed, and a Pratt & Whitney aircraft engine combustor is simulated as the second case. Effects of the interaction between turbulence and radiation and the influence of radiative heat losses on NO formation are discussed. The paper finishes with conclusions.

II. EXTENSION OF THE FPV MODEL TO ACCOUNT FOR RADIATION

The study of competing time scales in turbulent reacting flows is important for the quantification of the dynamics of the relevant physical phenomena. Such a time scale analysis for a piloted jet flame configuration is presented in the next section, which emphasizes the wide dynamical range be-

tween mixing, chemical reaction, and radiation. Compared to the chemical reaction of major species, it will be shown that radiation and NO formation are relatively slow processes which require the consideration of transient effects. Following the time scale analysis, a model extension is proposed in Sec. II B, which considers the slow radiative process. After the model presentation, the extended FPV model is applied in LES of a canonical test case and the interaction between turbulence, radiation, and chemistry is discussed.

A. Time scale analysis

Models employing the steady flamelet concept are usually inappropriate for the consideration of radiative effects. Reasons for this can be found by analyzing the time scale ratios associated with flamelet lifetime, chemical reaction, and radiation.[23] In an open jet flame, the flamelet lifetime can be related to the Lagrangian time:

$$\tau_u = \int_0^x (u(x')|_{Z_{st}})^{-1} dx', \qquad (10)$$

where u is the velocity component in the streamwise direction, and the notation $\cdot|_{Z_{st}}$ refers to data, that are conditioned on the stoichiometric mixture fraction. The chemical time scale associated with the formation of major product mass fractions can be defined as

$$\tau_C = \left. \frac{\Delta C}{\dot{\omega}_C} \right|_{Z_{st}}. \qquad (11)$$

Furthermore, the characteristic time scale for radiation may be estimated as[23]

$$\tau_r = \left. \frac{\rho c_p \Delta \Theta}{\dot{q}_R} \right|_{Z_{st}}, \qquad (12)$$

and a typical mixing time scale can be formed from the scalar dissipation rate:

$$\tau_m = \left. \frac{Z^2}{\chi_Z} \right|_{Z_{st}}. \qquad (13)$$

Note that in the present study, diffusion flames are considered, in which chemical reactions, heat release, and radiation are confined to a thin region around the stoichiometric condition. Therefore, the times scales for the characterization of these three processes are evaluated at a stoichiometric mixture.

From Eqs. (10)–(13), the following dimensionless groups can be formed:

$$\mathfrak{D}_C = \frac{\tau_u}{\tau_C}, \quad \mathfrak{R} = \frac{\tau_u}{\tau_r}, \quad \mathfrak{M} = \frac{\tau_u}{\tau_m}, \qquad (14)$$

where $\mathfrak{D}$ is the Damköhler number, and the time scale ratios characterizing radiative and mixing effects are denoted by $\mathfrak{R}$ and $\mathfrak{M}$, respectively. Typical time scale ratios, corresponding to the condition of the Sandia flame D experiment,[24,25] as function of the distance to the nozzle are shown in Fig. 3. The streamwise coordinate is non-dimensionalized with the nozzle diameter D. The velocity field, required for the evalu-
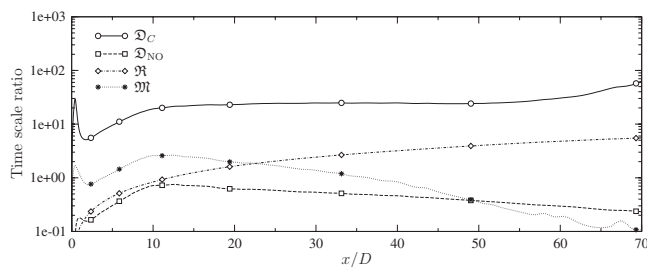
FIG. 3. Time scale ratios obtained from the unsteady flamelet simulation at conditions corresponding to the Sandia flame D experiment.

ation of τ_u in Eq. (10), and the mixture fraction-conditioned scalar dissipation rate are obtained from a LES, which is described in Secs. II D 2 and II D 3. From these data, an unsteady and a steady flamelet simulation were performed by solving Eqs. (1) and (2), respectively. Subsequently, the time scale ratios in Eq. (14) are evaluated, in which ΔC and $\Delta\Theta$ are defined to be the differences in progress variable and temperature between the unsteady and steady flamelet solutions for a given scalar dissipation rate. Therefore, τ_C and τ_r characterize the time which would be required to relax a flamelet to the steady-state condition. Figure 3 shows that $\mathfrak{R}$ monotonically increases with axial distance x. Since $\tau_r > \tau_u$ in the region up to $15D$ from the jet exit, radiation is essentially negligible in this area. With increasing downstream location, $\mathfrak{R}$ slowly increases, and the radiative time scale becomes comparable to the Lagrangian time scale.

The time scales between radiation and chemical reaction can be compared by forming the ratio $\mathfrak{D}_C/\mathfrak{R}$. The radiation time scale τ_r is at least an order of magnitude larger than τ_C throughout the simulation domain. Hence, while major species reached already a steady-state condition, radiation is still effective, resulting in a slow reduction in temperature and enthalpy.

This analysis illustrates the time scale difference in turbulent reacting flows and indicates that the interaction between turbulence, chemistry, and radiation can become relevant in certain technical applications. Therefore, the consideration of radiative heat losses in combustion models can be of importance for the accurate prediction of the turbulent flow field and the species distribution. The incorporation of radiation effects into the FPV model is described in the next section.

B. Model formulation

The discrepancy between the convective flamelet lifetime and the radiation time suggests that models of the form of Eq. (8) are not able to accurately account for radiation effects. In order to overcome this shortcoming, the enthalpy H, defined as

$$H = \int c_p d\Theta + \sum_\alpha \Delta H_{f,\alpha}^0 Y_\alpha, \qquad (15)$$

is introduced as an additional parameter, for which a transport equation is solved. Here, c_p is the specific heat at constant pressure and $\Delta H_{f,\alpha}^0$ is the heat of formation of species

α. Under the assumption of unity Lewis number, constant pressure, and negligible viscous dissipation effects, the conservation equation for H reduces to

$$\rho \mathcal{D}_t H = \nabla \cdot (\rho \alpha \nabla H) - \dot{q}_R, \qquad (16)$$

where $\dot{q}_R$ is the radiative sink term. After introducing H as an additional parameter in the state equation, Eq. (8), the extended form of the FPV model can be written as

$$\boldsymbol{\psi} = \mathcal{G}_{\boldsymbol{\psi}}^{\mathrm{e}}(Z, C, H), \qquad (17)$$

and the superscript e refers to the extended model. In this respect, the extended FPV model can be considered as a model in which all thermochemical quantities are represented by a three-dimensional manifold.

It is important to point out that Eq. (16) reduces to a conserved scalar transport equation in the case when radiation effects are negligible. Therefore, the model extension simplifies to Eq. (8). This appears to be a necessary condition in order to preserve model consistency, in the limit that radiation effects are insignificant. Note that similarly, an equation for the temperature could be solved instead of H. However, this equation contains a nonvanishing heat release source term, rendering the numerical solution somewhat more difficult.

In flames, radiation from the gas phase and soot are the main heat loss effects in the enthalpy equation. However, for diluted and weakly sooting flames, which are of interest here, soot radiation is typically insignificant and is therefore neglected in the following. For such flames, the radiative heat loss rate in Eq. (16) can be modeled in the optical thin limit as[26,27]

$$\dot{q}_R = 4\sigma(\Theta^4 - \Theta_\infty^4)\sum_\alpha p_\alpha a_\alpha, \qquad (18)$$

where p_α and a_α are the partial pressure and the Planck mean absorption coefficient of species α,[28] and Θ_∞ refers to the background temperature. This approach assumes that the flame radiates into a homogeneous environment with temperature Θ_∞ and that the absorption effects are insignificant within the flame. Note that because of the neglect of self-absorption effects, the model has the tendency to overpredict radiation effects.[29,30]

From the time scale analysis, discussed in Sec. II A, it is evident that the radiative heat loss rate cannot be taken from the steady flamelet solution. Instead, in the state-space region, in which radiation is important, transient flamelet equations are solved. The generation of the transient flamelet database is described in the next section.

C. Generation of the flamelet database

The thermochemical state of a flamelet is altered due to changes in the scalar dissipation rate and radiative heat loss effects. It was shown in Sec. II A that radiation is a rather inefficient process which results in a slow reduction in the flame temperature. The time scale analysis, presented in this section, also suggested that temperature-sensitive species cannot be predicted from the steady flamelet equations. Instead, in the extended FPV model, transient flamelet equa-
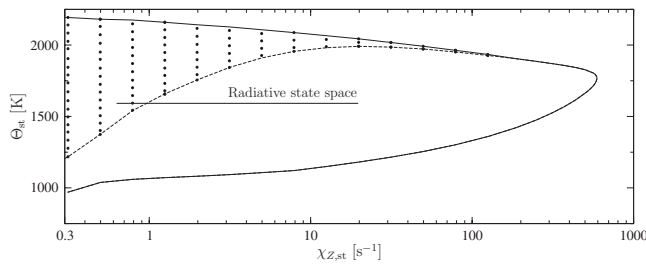
FIG. 4. Flamelet solution consisting of the upper and middle branches of the S-shaped curve. While the solid line corresponds to the solution of the steady flamelet equations without radiative heat losses, the steady flamelet temperature under consideration of radiation effects is shown by the dashed line. The symbols correspond to solutions of the unsteady flamelet equations with radiation.

tions, Eq. (1), are solved in the state space in which radiation is important (see Fig. 4). For the generation of the flamelet database, it is assumed that in this state space, the history of a flamelet is unimportant and that each flamelet trajectory can be decomposed into two components, namely, a change along the S-shape curve due to changes in χ_Z, followed by a variation due to heat loss effects. It will be shown in Sec. III B that this is a valid assumption for the temperature and all species that are formed on a sufficient fast time scale.

In the extended FPV model, the flamelet database is generated as follows. Beginning with the initial adiabatic steady-state solution, unsteady flamelet equations are solved under the consideration of radiative heat losses for a specified scalar dissipation rate. A sequence of unsteady flamelets along this trajectory is stored in a database, which is then used for the compilation of the flamelet library. After the solution of the unsteady flamelet equations reaches a steady state, which corresponds to the stable burning branch under the consideration of radiation, $\chi_{Z,st}$ is increased and the process is repeated.

In this context, it is important to point out that this modeling procedure is different from the unsteady flamelet model (USFM), in which the time-dependent scalar dissipation rate from the simulation is used to compute the flamelet solution.

The accessible flamelet space in the extended FPV model is shown in Fig. 4. Equation (12) shows that the radiation time scale is proportional to the temperature increment $\Delta\Theta$. For instance, a reduction in the peak temperature by $\Delta\Theta = 500$ K at $\chi_{Z,st} = 1$ s^{-1} by radiation would require a residence time that is an order of magnitude larger than the time required to reach the stoichiometric flame length. Therefore, the dashed line in Fig. 4 should only be considered as a lower bound on the burning flamelet solution. Intermediate flamelets between both stable branches are obtained from the unsteady flamelet equations. These flamelets, indicated by symbols, are included in the flamelet table.

D. LES application
1. LES model formulation

In LES, only information about filtered quantities is available. Therefore, the extended FPV model is further developed for application in LES, in which Favre-filtered conservation equations for mixture fraction, progress variable,

and enthalpy together with filtered equations for mass and momentum are solved. A Favre-filtered quantity of a scalar $\widetilde{\psi}$ is defined as

$$\widetilde{\psi}(t,\boldsymbol{x}) = \frac{1}{\overline{\rho}(t,\boldsymbol{x})}\int \rho(t,\boldsymbol{x}')\psi(t,\boldsymbol{x}')G(t,\boldsymbol{x}-\boldsymbol{x}')d\boldsymbol{x}', \quad (19)$$

where G is the LES filter kernel. Transport equations for $\widetilde{\boldsymbol{\xi}} = (\widetilde{Z},\widetilde{C},\widetilde{H})^{\mathsf{T}}$ can be written as

$$\overline{\rho}\widetilde{D}_t\widetilde{\boldsymbol{\xi}} = \nabla\cdot(\overline{\rho}\widetilde{\alpha}\,\nabla\,\widetilde{\boldsymbol{\xi}}) + \nabla\cdot\underline{\overline{\underline{\tau}}}^{\mathrm{res}} + \overline{\boldsymbol{q}}, \quad (20)$$

where $\widetilde{D}_t = \partial_t + \widetilde{\boldsymbol{u}}\cdot\nabla$, $\overline{\boldsymbol{q}} = (0,\overline{\rho}\widetilde{\omega}_C,\overline{q}_R)^{\mathsf{T}}$, $\underline{\overline{\underline{\tau}}}^{\mathrm{res}} = (\overline{\boldsymbol{\tau}}_Z^{\mathrm{res}},\overline{\boldsymbol{\tau}}_C^{\mathrm{res}},\overline{\boldsymbol{\tau}}_H^{\mathrm{res}})^{\mathsf{T}}$, with $\overline{\boldsymbol{\tau}}_\xi^{\mathrm{res}} = \overline{\rho}(\widetilde{\boldsymbol{u}}\widetilde{\xi} - \widetilde{\boldsymbol{u}\xi})$. The residual stresses and scalar fluxes that appear in the transport equations after filtering are modeled by a dynamic procedure and the residual scalar variance of the mixture fraction is obtained from an algebraic model.[31]

A presumed PDF is employed to express the state relation in Eq. (17) in terms of Favre-averaged quantities. For this, the mixture fraction-independent parameters, defined as $\Lambda = C|Z_{st}$ and $\Phi = H|Z_{st}$, which uniquely identify each flamelet, are introduced. Then, the flamelet library can be written as

$$\boldsymbol{\psi} = \mathcal{F}_{\boldsymbol{\psi}}^{\mathrm{e}}(Z,\Lambda,\Phi), \quad (21)$$

and $\widetilde{\boldsymbol{\psi}}$ is obtained from

$$\widetilde{\boldsymbol{\psi}} = \int\int\int \mathcal{F}_{\boldsymbol{\psi}}^{\mathrm{e}}(Z,\Lambda,\Phi)\widetilde{P}(Z,\Lambda,\Phi)dZd\Lambda d\Phi. \quad (22)$$

The statistical independence between Z, Λ, and Φ results in the simplification of the model for the joint PDF, which is here modeled as

$$\widetilde{P}(Z,\Lambda,\Phi) = \beta(Z;\widetilde{Z},\widetilde{Z''^2})\delta(\Lambda-\widetilde{\Lambda})\delta(\Phi-\widetilde{\Phi}), \quad (23)$$

where β and δ denote the beta distribution and Dirac delta function, respectively. With this, $\widetilde{\boldsymbol{\psi}}$ can formally be written as

$$\widetilde{\boldsymbol{\psi}} = \widetilde{\mathcal{F}}_{\boldsymbol{\psi}}^{\mathrm{e}}(\widetilde{Z},\widetilde{Z''^2},\widetilde{\Lambda},\widetilde{\Phi}). \quad (24)$$

By assuming that a unique inversion of $\widetilde{\mathcal{F}}_C^{\mathrm{e}}$ and $\widetilde{\mathcal{F}}_H^{\mathrm{e}}$ exists, $\widetilde{\Lambda}$ and $\widetilde{\Phi}$ in Eq. (24) can be eliminated by inverting this flamelet table. All thermochemical quantities can then be expressed in terms of only $\widetilde{Z}$, $\widetilde{Z''^2}$, $\widetilde{C}$, and $\widetilde{H}$ as

$$\widetilde{\boldsymbol{\psi}} = \widetilde{\mathcal{G}}_{\boldsymbol{\psi}}^{\mathrm{e}}(\widetilde{Z},\widetilde{Z''^2},\widetilde{C},\widetilde{H}). \quad (25)$$

Note that this relation corresponds to the state equation (17), expressed in terms of Favre-averaged quantities. In the following, the library is discretized with 100, 100, and 75 uniformly distributed grid points in the $\widetilde{Z}$, $\widetilde{C}$, and $\widetilde{H}$ directions, respectively. For the $\widetilde{Z''^2}$ direction, 25 points are used, and the grid spacing follows a geometric growth law.

The extended FPV model is applied in LES of Sandia flame D in the next section, and the effect of radiation on statistical flow field quantities is discussed.
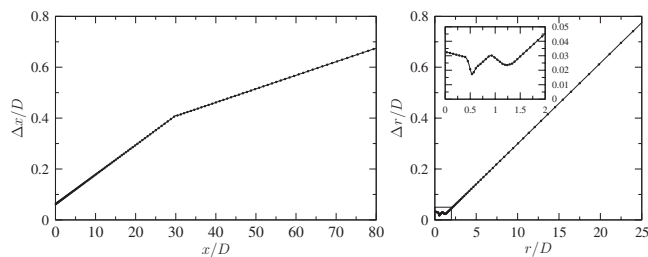
FIG. 5. LES grid stretching diagram for the Sandia flame D simulation: (left) axial direction; (right) radial direction. The inset in the right graph shows a zoom of the grid around the fuel nozzle. Only every second grid point is shown by the symbols.

2. Experimental configuration and numerical setup

The extended FPV model and the NO model, which is described in Sec. III, are applied in a LES of Sandia flame D. In the Sandia flame D experiment, a piloted partially pre-mixed methane/air diffusion flame at a Reynolds number of 22 400 was investigated.[24,25] The Reynolds number is based on the nozzle diameter, jet bulk exit velocity, and kinematic viscosity of the fuel jet. The central jet nozzle has a diameter of $D=7.2$ mm and the annular pilot nozzle diameter is 18.2 mm. Oxidizer air at 291 K is supplied in a coflow. The fuel jet velocity is $U_J=49.6(\pm 2)$ m/s and the coflow velocity is $0.9(\pm 0.05)$ m/s. The jet fluid consists of a mixture of methane and air in a volumetric ratio of 1:3 with a stoichiometric mixture fraction of $Z_{st}=0.351$. The pilot stream is a lean premixed gas mixture of C_2H_2, H_2, CO_2, N_2, and air with an equivalence ratio of 0.77 and a similar equilibrium composition as the jet fuel with $Z=0.271$. It has been reported that this flame burns as a diffusion flame and exhibits no significant premixed reaction zone in the fuel-rich region. Point measurements were obtained at streamwise locations $x/D=7.5$, 15, 30, and 45. The statistical errors of the measurements for the mean major species and temperature have been reported to be below 5% and those for CO are below 10%.

The Favre-filtered conservation equations for mass, momentum, mixture fraction, progress variable, and enthalpy are solved in a cylindrical coordinate system $\boldsymbol{x}=(r,\varphi,x)^{\mathsf{T}}$. The geometry has been nondimensionalized by the jet nozzle diameter D and the computational domain is $27D \times 2\pi \times 80D$ in the radial, circumferential, and axial directions, respectively. The radial direction is discretized by 160 unevenly spaced grid points concentrated in the fuel nozzle. For the discretization of the jet radius, 18 grid points are used. The grid in the axial direction uses 256 points and is, beginning at the nozzle exit, stretched downstream. The circumferential direction is equally spaced and uses 64 points. The total number of grid points used for the simulation is approximately 2.6×10^6. The corresponding grid spacing diagrams in the axial and radial directions are shown in Fig. 5. The nondimensional minimum and maximum filter widths in the domain are $\Delta_{\min}=0.04$ (shear layer at the nozzle lip line) and $\Delta_{\max}=1.1$ (outermost grid cell at the outflow plane). The turbulent inlet velocity profile is generated by separately performing a periodic pipe flow simulation by enforcing the experimentally determined axial mean velocity profile. Con-

vective outflow conditions are used at the outlet and slip-free boundary conditions are employed at the radial boundaries. The numerical simulation is run over ten flow-through times to obtain a statistically stationary flow field. Statistical results are subsequently computed over ten flow-through times, which corresponds to 800 nondimensional time units or 116 ms physical time. It was found that a further increase in the sampling interval did not change the statistical results.

The computed mean and resolved variances are obtained by averaging in the temporal and azimuthal directions:

$$\langle \widetilde{\psi} \rangle(x,r) = \frac{1}{2\pi T} \int_{t}^{t+T} \int_{0}^{2\pi} \widetilde{\psi}(t,x,r,\varphi) d\varphi dt, \tag{26a}$$

$$\langle \widetilde{\psi}_{<}''^2 \rangle(x,r) = \frac{1}{2\pi T} \int_{t}^{t+T} \int_{0}^{2\pi} [\widetilde{\psi}(t,x,r,\varphi) - \langle \widetilde{\psi} \rangle(x,r)]^2 d\varphi dt, \tag{26b}$$

where $\langle \widetilde{\psi} \rangle$ denotes the mean value of $\widetilde{\psi}$ and $\langle \widetilde{\psi}_{<}''^2 \rangle$ is the resolved variance.

3. Sandia flame D results

In Sec. II D 1, the FPV model has been extended to account for radiative heat loss effects. In this model, the Favre-filtered enthalpy is introduced as an additional scalar for the parametrization of all thermochemical quantities, and the radiative source term is modeled in the optically thin limit.

In the following, the interaction between turbulence, radiation, and chemistry in the Sandia flame D is investigated. For this, two numerical simulations are conducted, which are schematically shown in Figs. 6(a) and 6(b). In these diagrams, the white boxes refer to the solutions of the governing equations for the flow field, scalar field, and enthalpy, respectively, and the gray boxes in each diagram denote the interface to the chemistry library.

The first simulation [Fig. 6(a)] corresponds to the original FPV formulation by Pierce and Moin,[16] in which only the interaction between turbulence and chemistry is considered, and radiation effects are neglected. The second simulation [Fig. 6(b)] employs the extended FPV model of Sec. II D 1, which accounts for the coupling between turbulence, chemistry, and radiation. To quantify the interaction between turbulence and radiation in isolation, the data of the first simulation are postprocessed by evaluating only the flame temperature from the extended FPV model [Fig. 6(c)]. Thus, differences in the flame temperature between the models shown in Figs. 6(a) and 6(b) are due to the turbulence/chemistry/radiation interaction, and differences between the models in Figs. 6(a) and 6(c) can be attributed to radiative heat loss effects.

Centerline profiles for the mean and rms values of axial velocity, mixture fraction, and temperature are shown in Fig. 7, and statistical results are obtained by averaging over a time interval of ten flow-through times to obtain fully converged statistical data. The comparison between the adiabatic and radiative calculations shows only minor differences in the evolution of the mean and rms axial velocities. This sug-
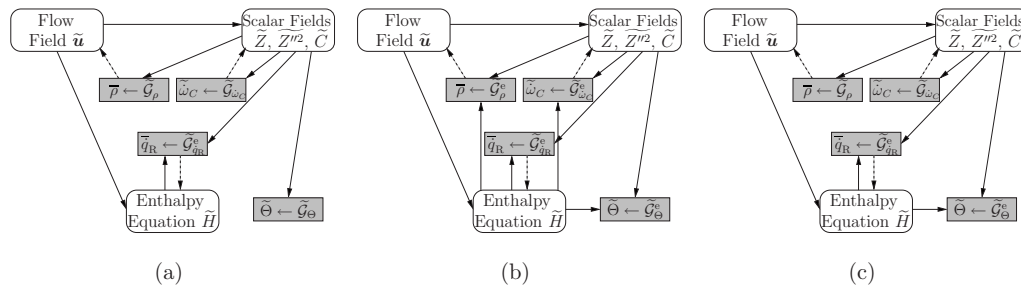
FIG. 6. Schematic diagrams which summarize the numerical simulations to quantify the interaction between turbulence, chemistry, and radiation in Sandia flame D: (a) adiabatic simulation using the original FPV model (Ref. 16), which considers only the interaction between turbulence and chemistry; (b) extended FPV model, Eq. (25), which accounts for the interaction between turbulence, chemistry, and radiation; (c) adiabatic FPV simulation, in which effects of the coupling between turbulence and radiation are separately analyzed by evaluation of only the temperature from the extended FPV model.

gests that radiation itself and its interaction with turbulence have only an insignificant effect on the velocity field in the present configuration.

Statistical results of the mixture fraction are shown in the middle row of Fig. 7. While the predicted mean mixture fraction profile from the radiative simulation is in good agreement with the experimental data, the adiabatic simulation overpredicts the mean mixture fraction for $x/D \gtrsim 20$. The profiles for the mixture fraction fluctuations, shown in the right column, exhibit only minor differences between both simulations.

The time scale analysis, shown in Fig. 3, suggests that radiation effects start to become important for $x/D > 15$. However, the predicted temperature profiles from the adiabatic and radiative calculations are virtually identical up to the location of the stoichiometric flame length, which is defined as $L_{st} = \{x | \langle \tilde{Z} \rangle (x,0) = Z_{st}\}$. For the region above L_{st}, the adiabatic simulation (dashed line) overpredicts the tempera-

ture by approximately $100-150$ K. By accounting only for heat loss effects through the radiation sink term in the enthalpy equation without considering the turbulence/radiation interaction, the temperature decreases by approximately 80 K in the fuel-lean region of the flame. The complete consideration of the interaction between turbulence, radiation, and chemistry through the extended FPV model yields to an additional temperature decrease of about 60 K. This shows that the coupling between these three thermophysicochemical processes is important for the accurate prediction of the flame temperature.

In order to obtain a better understanding of the radiation effect on the temperature, it is helpful to plot the mean temperature as a function of mean mixture fraction, which is shown in Fig. 8. By approximating the temperature differential as $d\langle \tilde{\Theta} \rangle = \partial_{\langle \tilde{Z} \rangle} \langle \tilde{\Theta} \rangle d\langle \tilde{Z} \rangle$, with $\partial_{\langle \tilde{Z} \rangle} \langle \tilde{\Theta} \rangle |_{lean} \approx 5700$ K and $\partial_{\langle \tilde{Z} \rangle} \langle \tilde{\Theta} \rangle |_{rich} \approx 3100$ K, the effect of the overprediction of the
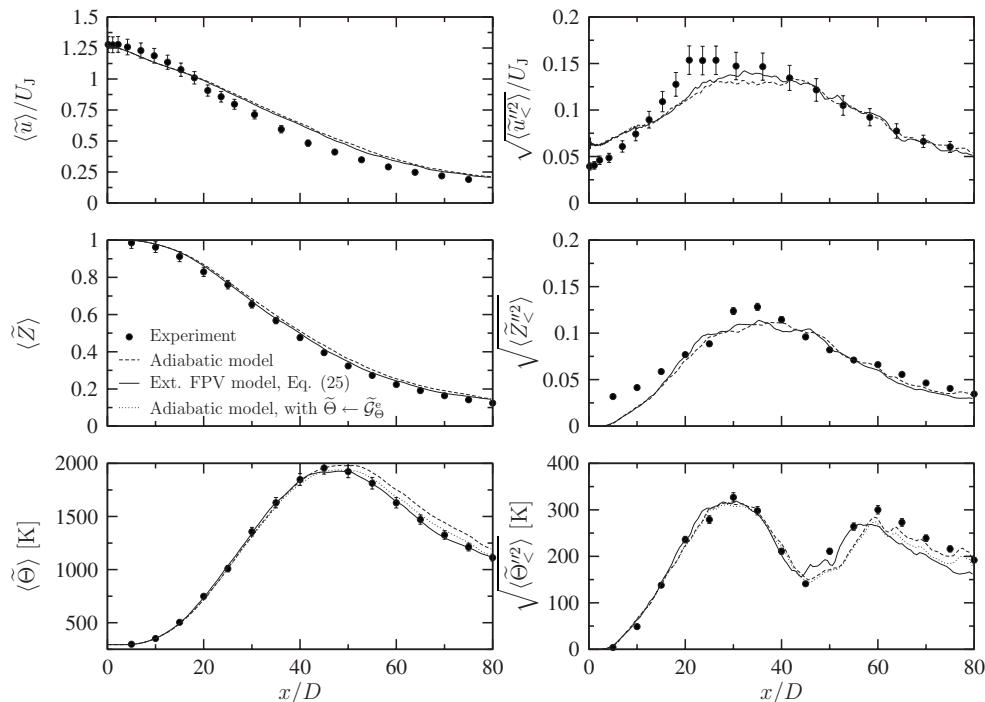

FIG. 7. Comparison of measured (symbols) and calculated (solid lines) mean and rms statistics of axial velocity, mixture fraction, and temperature along the centerline for Sandia flame D. Experimental data are plotted with estimated uncertainties.
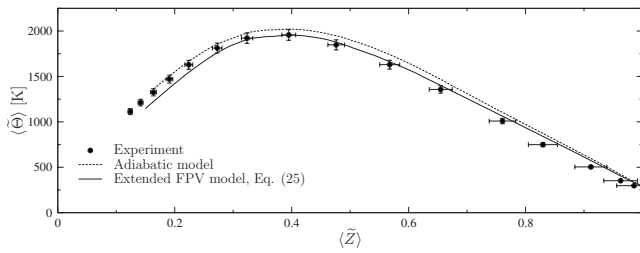
FIG. 8. Comparison of the predicted mean temperature as a function of $\langle \tilde{Z} \rangle$ along the centerline with experimental data.

mixture fraction in the adiabatic simulation becomes apparent. From this, the pronounced temperature sensitivity on the fuel-lean side is evident, which is approximately a factor of 2 higher than that on the fuel-rich side of the flame.

Figure 8 shows that the mixture fraction-conditioned temperature profile obtained from the radiative simulation is in better agreement with experimental data compared to the adiabatic simulation. It can be seen that radiation is also effective in the fuel-rich part of the flame, which is in agreement with the expectation following the time scale analysis. The temperature on the fuel-lean side is underpredicted. It is important to understand that this region corresponds to the flame location above L_{st} and large residence time. The underprediction of the temperature can be attributed to the known fact that the optically thin radiation model typically overestimates the fraction of radiative heat loss, which has also been observed in calculations using the TPDF method and the CMC model.[29,30,32,33]

III. MODEL FOR THE PREDICTION OF NITRIC OXIDE FORMATION

In this section, a model for the prediction of the nitric oxide formation is developed. The strong temperature sensitivity of the NO formation requires the accurate description of the instantaneous temperature field in a flame under the consideration of radiative heat loss effects, which was addressed in Sec. II B.

In the first part of this section, a model for the NO formation is presented. The performance of the model is then scrutinized in a model analysis for the three relevant NO formation mechanisms, namely, thermal, nitrous oxide, and prompt mechanisms. The individual assumptions of the model are assessed against results obtained from an unsteady flamelet model. Following this model analysis, a closure model for application in LES is developed. This model is then applied in LES of Sandia flame D and a Pratt & Whitney aircraft engine combustor configuration.

A. Model formulation

Similar to the radiation process, NO formation, particularly via the thermal mechanism, occurs on a relatively long time scale τ_{NO} compared to the flamelet lifetime. As an example, the timescale ratio $\mathfrak{D}_{\text{NO}} = \tau_u / \tau_{\text{NO}}$, obtained from a numerical simulation of Sandia flame D, is shown in Fig. 3. A comparison of the chemical time scales of the major species formation to the NO formation indicates that τ_{NO} is typically

more than an order of magnitude larger than τ_C. This observation suggests that NO is not in steady state, and a steady-state assumption will consequently result in considerable overpredictions of NO.

The slow spatial and temporal formation and consumption of NO are described in the present model by the separate solution of a transport equation for the NO mass fraction Y_{NO}. Under the assumption of equal species diffusivities, this equation can be written as

$$\rho \mathcal{D}_t Y_{\text{NO}} = \nabla \cdot (\rho \alpha \nabla Y_{\text{NO}}) + \rho \dot{\omega}_{\text{NO}}. \tag{27}$$

In the following, we will extract the chemical production rate of NO from the extended FPV model, i.e., $\dot{\omega}_{\text{NO}} = \mathcal{G}^{\text{e}}_{\dot{\omega}_{\text{NO}}}(Z, C, H)$. This, however, requires special attention and is explained by considering the following elementary model reaction:

$$A + B \underset{k_b}{\overset{k_f}{\rightleftharpoons}} NO + D,$$
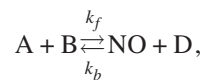
in which species A and B react to form products NO and D. Here, k_f and k_b denote the rate coefficients of the forward and backward reactions, respectively. For this reaction, the chemical reaction rate of NO can be written as

$$\dot{\omega}_{\text{NO}} = \dot{\omega}^+_{\text{NO}} + \dot{\omega}^-_{\text{NO}}, \tag{28}$$

with the production and consumption rates of the forms

$$\dot{\omega}^+_{\text{NO}} = \frac{W_{\text{NO}}}{\rho^{\text{FPV}}} k_f^{\text{FPV}} \left(\frac{\rho^{\text{FPV}} Y_A^{\text{FPV}}}{W_A} \right) \left(\frac{\rho^{\text{FPV}} Y_B^{\text{FPV}}}{W_B} \right), \tag{29a}$$

$$\dot{\omega}^-_{\text{NO}} = -Y_{\text{NO}}^{\text{FPV}} k_b^{\text{FPV}} \left(\frac{\rho^{\text{FPV}} Y_D^{\text{FPV}}}{W_D} \right). \tag{29b}$$

Since reaction rates will be taken from the flamelet library, all species in Eqs. (29a) and (29b) correspond to the conditions of the flamelet library and are explicitly denoted by the superscript FPV.

In the following, it is assumed that all species except NO are formed on relatively short time scales, and can therefore be represented by the FPV library. Since $\dot{\omega}^-_{\text{NO}}$ is a function of $Y_{\text{NO}}^{\text{FPV}}$, the consumption rate is adjusted by using the computed NO mass fraction from Eq. (27). Thus, the modeled NO production rate can be written as

$$\dot{\omega}_{\text{NO}} = \dot{\omega}^+_{\text{NO}} + Y_{\text{NO}} \frac{\dot{\omega}^-_{\text{NO}}}{Y_{\text{NO}}^{\text{FPV}}}. \tag{30}$$

It is interesting to note that this model converges to that of the unsteady flamelet model, since in this case, $Y_{\text{NO}} = Y_{\text{NO}}^{\text{FPV}}$, ensuring model consistency.

Although the model given by Eqs. (29a) and (29b) was written here for a simple one-step NO formation reaction, it can be used for general detailed reaction schemes by expressing $\dot{\omega}^+_{\text{NO}}$ and $\dot{\omega}^-_{\text{NO}}$ in terms of the total NO production and consumption rates, respectively. Note also that the model for the NO consumption rate as given above considers only reactions which are first order in NO. This model, however, can be extended by expanding $\dot{\omega}^-_{\text{NO}}$ in terms of its corresponding reaction order.
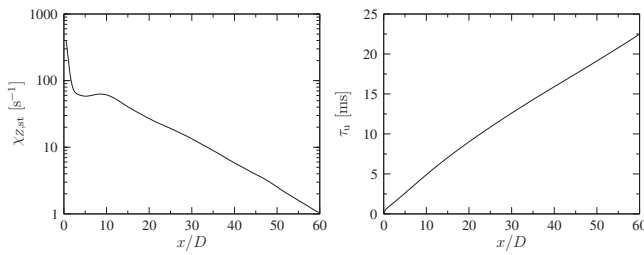
FIG. 9. Axial evolution of stoichiometric scalar dissipation rate (left) and flamelet lifetime (right) obtained from LES.

B. Model analysis

1. Formulation of the model problem

The model for the prediction of the NO mass fraction, consisting of Eqs. (27) and (30), is investigated in a model analysis. In particular, the three dominant NO formation mechanisms, namely, the thermal, N_2O, and prompt mechanisms, are separately analyzed here.

Because of lack of detailed experimental data that distinguish the individual NO formation pathways, results obtained from an unsteady flamelet simulation are used as a reference. This is mainly motivated by the fact that the unsteady model yields accurate predictions for NO and other species.[34,35] The solution obtained from the unsteady flamelet model can also be seen as the target for the present model, since it was shown in the previous section that the results should be the same under the assumption that all species are in steady state except for NO.

A simplified but realistic model case has been devised for the model analysis. This test case is based on the Sandia flame D configuration. However, in order to separately assess the proposed model and the underlying model assumptions, effects of turbulence are not yet considered. The test case is described in the following.

In the first step, a representative unsteady flamelet is solved subject to a prescribed scalar dissipation rate $\chi_{Z,st}(\tau_u)$. The convective time scale $\tau_u(x)$ and stoichiometric scalar dissipation rate $\chi_{Z,st}(\tau_u)$, shown in Fig. 9, are computed from the LES, which was described in Secs. II D 2 and II D 3. The functional form of the scalar dissipation rate is then obtained from the following analytical expression:[3]

$$\chi_Z(Z) = \chi_{Z,st} \exp\{2([\mathrm{erfc}^{-1}(2Z_{st})]^2 - [\mathrm{erfc}^{-1}(2Z)]^2)\}. \tag{31}$$

Since no further modeling is involved in this equation, its solution is referred to as the reference solution and is denoted in the following by USFM.

In this context, it is important to point out that a pilot is used to stabilize the flame. The pilot not only provides a constant source of heat and radicals but also reduces the scalar dissipation rate on the fuel-lean side of the flame. The effect of the differences in the dissipation rate profiles on the temperature and NO mole fraction are shown in Fig. 10. From this figure, minor differences in the temperature profile at the first measurement station can be seen; however, the peak NO mole fraction is approximately 10 ppm higher in the simulation that employs the analytical expression for χ_Z.
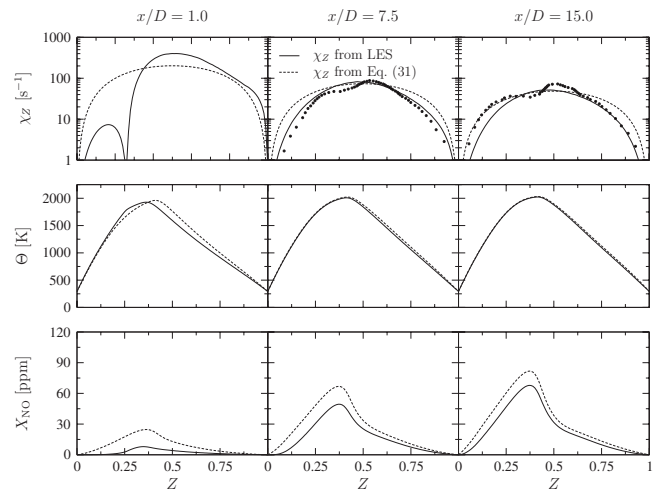

FIG. 10. Comparison of the flamelet structure for temperature and NO mole fraction at three different locations in the jet obtained from an unsteady flamelet simulation for two different profiles of the scalar dissipation rate. For reference, measurements of the scalar dissipation rate for locations $x/D = 7.5$ and 15 are shown by symbols (Ref. 47).

In the following step, Eq. (27) is transformed into flamelet space, viz.,

$$\partial_t Y_{NO} - \frac{1}{2}\chi_Z(\tau_u)\partial_Z^2 Y_{NO} = \dot{\omega}_{NO}, \tag{32}$$

with $\dot{\omega}_{NO}$ from Eq. (30) and $\dot{\omega}_{NO}^+$, $\dot{\omega}_{NO}^-$, and Y_{NO}^{FPV} are obtained from the extended FPV library $\mathcal{G}^e$. The mixture fraction, progress variable, and enthalpy which are input parameters to this library are taken from the unsteady flamelet simulation. For comparison, profiles of Y_{NO}^{FPV} from the flamelet library are also presented in the following.

The chemistry is described by the GRI 2.11 mechanism.[36] From this, three separate mechanism files are compiled by eliminating reactions that are not part of the individual NO formation mechanisms.

In the derivation of the model, essentially four assumptions have implicitly been invoked. These assumptions are summarized here:

(1) A particular flamelet is uniquely identified by Z, C, and H. This essentially reflects the FPV assumption.

(2) In Eq. (30), it is assumed that all species, except NO, are formed on a sufficiently short time scale and can therefore be represented by the species distribution in the flamelet table.

(3) The unsteady flamelets solved for the compilation of the flamelet library evolve along a different trajectory than the representative unsteady flamelet parametrized by $\tau_u(x)$ and $\chi_{Z,st}(\tau_u(x))$. This implicitly assumes that the particular flamelet history is of less importance.

(4) The model for the NO consumption rate in Eq. (30) only considers first-order NO consumption reactions. This, however, can be remedied in a straightforward way but was not further investigated here.

Despite the fact that these assumptions are not separately addressed here, their integral effect on the NO formation is analyzed in the following.
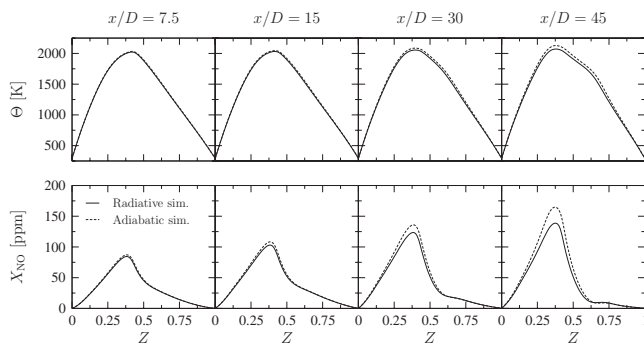
FIG. 11. Effects of radiation on flamelet temperature and NO mole fraction.

FIG. 12. Comparison of the model results for the Zeldovich mechanism at four different axial locations.

2. Effect of radiation

The effect of radiation on the flame temperature and NO mole fraction is shown in Fig. 11. Two representative flamelets are solved subject to the transient scalar dissipation rate from the LES. The dashed line represents the adiabatic solution, and the profiles shown by the solid lines account for radiation. Radiation in the optically thin limit leads to a decrease in the peak temperature by 70 K at $x/D = 45$ and a reduction in NO by 20% to 140 ppm.

3. Zeldovich mechanism

The main source of NO in the combustion of nitrogen-free fuel and air is considered to be the Zeldovich mechanism[37] if the temperature is sufficiently high. The principal reactions are given in the Appendix, Sec. 1, and a corresponding reaction flux diagram is shown in Fig. 23. This mechanism is usually unimportant at temperatures below 1800 K, which is due to the fact that the rate-limiting reaction (A1) has a large activation energy.

The GRI 2.11 mechanism is reduced so that all nitrogen-related reactions, except reactions (A1)–(A3), are deleted. By using this simplified mechanism, flamelets are generated and compiled into a flamelet library. This library, parametrized by Z, C, and H, is then used in the NO model.

Results obtained from the NO model are compared to data from the representative unsteady flamelet model in Fig. 12. Profiles for the NO mole fraction and the contributions to the reaction rate due to production and consumption are shown at four different axial locations. The NO mole fraction is shown in the top row. Compared to the unsteady results, X_{NO}^{FPV} from the extended flamelet library is overpredicted by a factor of 2 for all measurement locations. This can be attributed to the slow NO consumption rate and is discussed in more detail in Sec. III B 5. The slow increase in NO with increasing downstream distance is a manifestation of the large formation time of the thermal mechanism. Except for the last location, the model results can be considered to be in excellent agreement with the reference solution. The reason for the small overprediction at $x/D = 45$ can be attributed to the difference of the formation rates $\dot{\omega}_{NO}^{+}$ between both models. A comparison of the flame structure between both models showed differences in the O and N radical profiles. Particularly, the larger concentration of N in the extended FPV model on the fuel-rich side results in a larger production rate
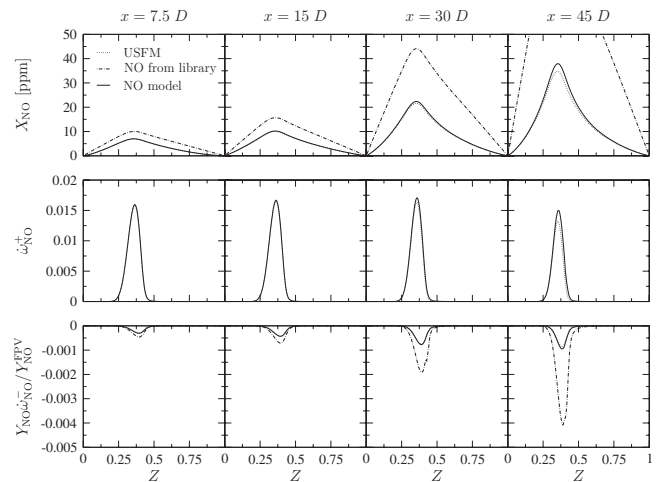
via reaction (A3). On the other hand, the peak O mass fraction in the FPV model is approximately 10% lower than in the representative unsteady flamelet model, resulting in a lower NO production rate from reaction (A1). However, since reactions (A1) and (A3) contribute in equal parts to the overall NO production, both effects nearly cancel.

The last row in Fig. 12 also shows a comparison between the modeled consumption rate and the consumption rate taken from the flamelet library. This shows that a rescaling of the NO consumption rate is a valid and necessary model component.

The effects of the formation rate and rescaled consumption rate on NO formation can be individually analyzed by writing the following zero-dimensional NO evolution equation:

$$d_t Y_{NO}(t) = \dot{\omega}_{NO}^{+} + Y_{NO}(t) \frac{\dot{\omega}_{NO}^{-}}{Y_{NO}^{FPV}} \quad \text{with } Y_{NO}(t=0) = Y_{NO}^{0}. \quad (33)$$

Here, it is assumed that $\dot{\omega}_{NO}^{+}$ and $\dot{\omega}_{NO}^{-}/Y_{NO}^{FPV}$ are independent of time, which is a reasonable assumption for the Zeldovich mechanism (see Fig. 12). The solution of this equation is

$$Y_{NO}(t) = -\frac{\dot{\omega}_{NO}^{+}}{\dot{\omega}_{NO}^{-}} Y_{NO}^{FPV} \left(1 - \exp\left\{ \frac{\dot{\omega}_{NO}^{-}}{Y_{NO}^{FPV}} t \right\} \right)$$
$$+ Y_{NO}^{0} \exp\left\{ \frac{\dot{\omega}_{NO}^{-}}{Y_{NO}^{FPV}} t \right\}, \quad (34)$$

with the equilibrium NO mass fraction:

$$\lim_{t \to \infty} Y_{NO}(t) = -\frac{\dot{\omega}_{NO}^{+}}{\dot{\omega}_{NO}^{-}} Y_{NO}^{FPV} \quad (35)$$

and the mean lifetime:

$$\tau = -\frac{Y_{NO}^{FPV}}{\dot{\omega}_{NO}^{-}}. \quad (36)$$

From Eqs. (35) and (36), the influence of the consumption rate on the temporal evolution of the NO mass fraction becomes apparent: The typically small consumption rate in the
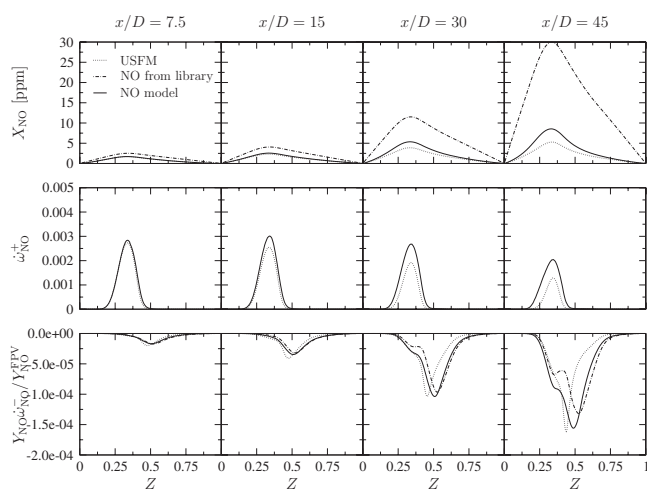
FIG. 13. Comparison of the model results for the N_2O mechanism at four different axial locations.

FIG. 14. Comparison of the model results for the prompt NO mechanism at four different axial locations.

Zeldovich mechanism not only results in a large equilibrium concentration of NO but also leads to a large mean lifetime.

4. Nitrous oxide mechanism

Nitrous oxide is mostly formed under fuel-lean and high pressure conditions. The principal N_2O reaction mechanism is shown in the Appendix together with a reaction flux diagram in Fig. 24. Note that the reactions describing the formation of the nitrogen-containing radicals are not given in the Appendix for brevity; they are, however, included in the employed mechanism file here.

A comparison of results obtained from the NO model with the unsteady flamelet data is shown in Fig. 13, and the computed NO mole fractions obtained from the models are presented in the top row. It is interesting to point out that the NO production via the N_2O mechanism is considerably smaller compared to that of the Zeldovich mechanism. The NO mole fraction predicted from the flamelet library is over-predicted by a factor of 6. The NO model results in a considerably better prediction of X_{NO}. The apparent overprediction of the model at the last two stations is attributed to higher values of the NO production rate compared to the representative unsteady flamelet model. The primary NO formation step in this mechanism is reaction (A9) with a small contribution from reaction (A5). A careful analysis of the flame structures showed that differences in the H radical profiles around the stoichiometric condition lead to higher values for $\dot{\omega}_{NO}^+$ and the consequent NO overprediction.

5. Prompt mechanism

The rapid formation of NO predominantly in the fuel-rich part of the flame on time scales shorter than that of the Zeldovich mechanism has been termed "prompt NO."[38] The primary initiation step in this mechanism is the reaction of molecular nitrogen with hydrocarbon radicals to form amino and cyano compounds via reactions (A24)–(A27) (see the Appendix). The dominant step in the considered mechanism is reaction (A26), and reactions (A24) and (A25) are typi-
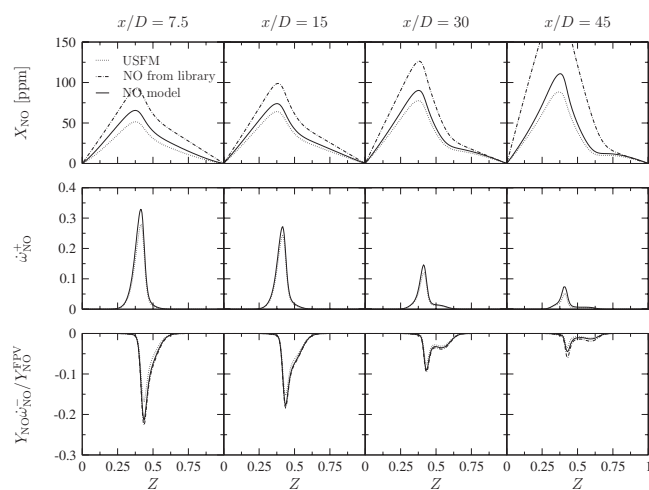
cally insignificant contributors to prompt NO due to their large activation energies.[39] In a sequence of reactions, hydrogen cyanide is then converted into NO.

Under fuel-rich conditions, it is observed that the NO concentration decreases relative to hydrogen cyanide.[39] This effect is termed "NO reburn" and is attributed to a decrease in the O-atom concentration, favoring reactions that convert CH_3 to CH_2 over the CH_3 oxidation reaction. This, in turn, allows the NO recycling reactions (A28)–(A31) to become more effective.

The relevant reaction sequence for the prompt NO mechanism is summarized in the Appendix. The reaction flux diagram for the fuel and oxidizer condition corresponding to the Sandia flame experiment and $\chi_{Z,st}=50$ s^{-1} is shown in Fig. 25.

The GRI 2.11 mechanism is reduced so that it includes only the nitrogen-related reactions of the Appendix. Flamelets are generated by using this reduced mechanism and are compiled into a library which is used here for the model analysis.

Results obtained from the model simulation are compared to reference data from the unsteady flamelet simulation in Fig. 14. Comparing first the peak NO mole fraction between all three mechanisms, it is apparent that the major NO contribution originates from the prompt mechanism. Only 25% of the NO is formed by the thermal mechanism, and less than 5% comes from the N_2O reaction pathway. Particularly, the relatively large ratio between prompt and thermal NO can be attributed to the partially premixed fuel composition, with a fuel-air equivalence ratio of $\phi=3.2$. The dilution of the fuel with air leads not only to a reduced formation of polycyclic aromatic hydrocarbons but also to a lower flame temperature due to the higher stoichiometric mixture, reducing the efficiency of the Zeldovich reaction mechanism.

The rapid formation of NO via the prompt path is also evident from Fig. 14. The unsteady flamelet model predicts a peak NO mole fraction of about 50 ppm at $x/D=7.5$, which increases to 90 ppm at the last measurement station. It is interesting to compare this overall increase by 80% to that of
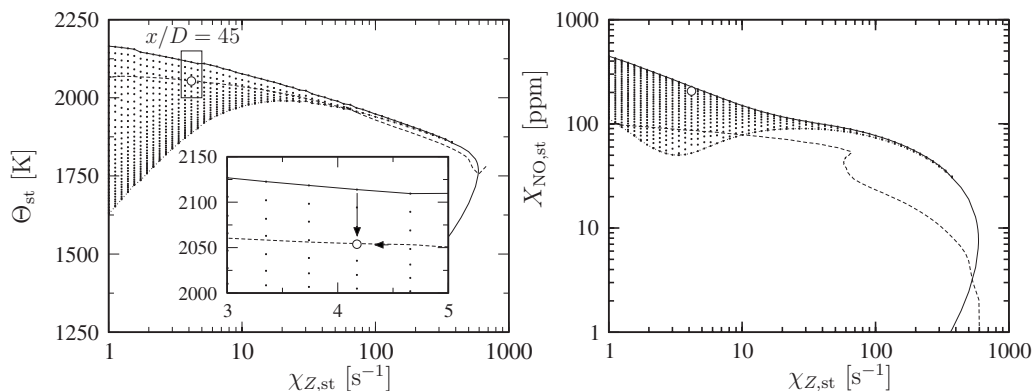
FIG. 15. Trajectories of representative unsteady flamelets (dashed lines) and unsteady flamelet equation for generation of flamelet library (vertical arrow); the small symbols denote unsteady flamelet solutions for the generation of flamelet library.

the Zeldovich mechanism in Fig. 12, where the peak NO mole fraction increases by a factor of 4 over the same axial distance.

The solid line in the upper row of Fig. 14 shows the NO mole fraction obtained from the NO model. This result must be compared to profiles from the representative unsteady flamelet solution (dashed line). The NO model overpredicts the peak NO mole fraction by approximately 10 ppm at the first three measurement stations and 20 ppm at $x/D=45$. This corresponds to a model error of less than 25%. Before the reason for this discrepancy is analyzed in more detail, the NO profiles directly extracted from the flamelet library are compared to the reference results from the unsteady flamelet simulation. These data are shown by the dotted lines. The overprediction in NO by as much as 130% at $x/D=45$ suggests that prompt NO requires the consideration of flame unsteadiness. This conclusion is particularly interesting since it is well known that prompt NO is rapidly formed, and one might consequently expect that its consumption is also a rapid process.

Here, it is emphasized that the flamelet library consists of a set of unsteady flamelets which are generated in the following way: Beginning from an initial condition, corresponding to the steady flamelet solution without radiative heat losses, the unsteady flamelet equations are solved for a given $\chi_{Z,st}$. Since the scalar dissipation rate is kept constant, the trajectory which is described by the solution of the unsteady flamelet equations corresponds to a vertical line in flamelet space. One such trajectory is shown by the vertical arrow in the inset of Fig. 15. The small symbols correspond to unsteady flamelet solutions. Additionally, the trajectory described by the representative unsteady flamelet as a function of the time-dependent scalar dissipation rate is shown by the dashed curve. The open symbol corresponds to a particular flamelet in the library with identical parametrization (viz., C and H) to that of the representative unsteady flamelet at $\chi_{Z,st}=4.1$ s^{-1} and corresponds to the axial location of $x/D=45$. It is interesting to point out that the time at which this flame state is reached differs by almost a factor of 2 between the two solution trajectories (9.5 ms for the solution along the vertical trajectory and 17.7 ms for the representative unsteady flamelet solution). Despite this difference, the tem-

perature, shown in the left panel of Fig. 15, and also the major species profiles relax to a similar solution. This shows that the path along which an unsteady flamelet evolves is of secondary importance for the major species formation. However, this statement is not true anymore in the case when a flamelet experiences rapid changes in the scalar dissipation rate. Examples are highly stretched flame regions which can lead to local flame extinction. Therefore, it is required that $\chi_{Z,st}/\dot{\chi}_{Z,st} > \tau_\psi$, where τ_ψ corresponds to the characteristic time scale for the formation of a major species ψ.

The right panel of Fig. 15 shows the NO mole fraction together with the trajectory of the representative unsteady flamelet in $\chi_{Z,st}-X_{NO,st}$ space (dashed line). The open symbol corresponds to the NO value from the flamelet library and indicates the slow time scale of NO consumption in the prompt mechanism. The flamelet library is composed of unsteady flamelet solutions under the influence of radiation starting from the adiabatic steady-state solution at the corresponding scalar dissipation rate and ending at the radiating steady-state value. The NO mole fraction decreases from an adiabatic steady state-value of 227 ppm to 205 ppm over a duration of 9.5 ms. In order to reach a value corresponding to that of the representative unsteady flamelet model of 90 ppm, a residence time of 80 ms would be required.

The trajectory of the representative unsteady flamelet also shows that after an initial transition time (corresponding to $x<8.5D$), the NO mole fraction reaches a nearly quasi-steady state and increases only slowly with increasing flamelet lifetime.

Next, the difference in the NO profiles between the results of the representative unsteady flamelet simulation and the NO model are discussed. A reaction flux analysis showed that reactions (A3) and (A31) are the primary channels for NO formation. In the nozzle-near region, 85% of the NO is formed through reaction (A3) and 10% comes from reaction (A31). With increasing downstream distance, the contribution of reaction (A3) decreases by 20% and reaction (A31) amounts to approximately 25% of the overall NO concentration. Since the NO formation is mainly governed by these two reactions, its formation rate can be approximated by

$$\dot{\omega}_{NO}^{+} = [N][OH]k_f^{A3} + [H][HCNO]k_b^{A31}. \tag{37}$$

The overprediction of NO as seen in Fig. 14 can be attributed to the difference in the N profiles between the representative unsteady flamelet model and the NO model. The nitrogen radical profile is 50% larger in the extended FPV model compared to that of the representative unsteady flamelet model. The other minor species OH, H, and HCNO agree well between both models.

In the present case, the most important NO consumption step in the prompt NO mechanism is reaction (A36) with the consumption rate:

$$\dot{\omega}_{NO}^{-} = -[NO][HCCO]k_f^{A36}, \tag{38}$$

and the discrepancy of the consumption rate is attributed to differences in the HCCO profiles and also effects of rescaling.

IV. LES APPLICATION

In a LES application, a transport equation for the Favre-filtered NO mass fraction $\widetilde{Y}_{NO}$ is solved. After multiplying Eq. (27) with the LES filter kernel G and spatial integration, this equation can be written as

$$\bar{\rho}\widetilde{D}_t\widetilde{Y}_{NO} = \nabla \cdot (\bar{\rho}\widetilde{\alpha}\nabla\widetilde{Y}_{NO}) + \nabla \cdot \overline{\tau}_{NO}^{res} + \bar{\rho}\widetilde{\omega}_{NO}, \tag{39}$$

and with the definition

$$\dot{\varpi}_{NO} \equiv \frac{\dot{\omega}_{NO}^{-}}{Y_{NO}^{FPV}}, \tag{40}$$

the filtered production rate is modeled as

$$\widetilde{\omega}_{NO} = \widetilde{\omega}_{NO}^{+} + \widetilde{Y}_{NO}\widetilde{\varpi}_{NO} + \widetilde{Y_{NO}''\varpi_{NO}''}, \tag{41}$$

where cross terms are neglected. The last term on the right hand side accounts for residual scale correlations between the computed NO mass fraction and consumption rate. This term cannot directly be obtained from the flamelet library and requires modeling. In this work, closure is obtained by assuming scale similarity between Y_{NO} and Y_{NO}^{FPV}, which can be written as

$$\frac{\widetilde{Y}_{NO}}{\widetilde{Y}_{NO}^{FPV}} = \frac{Y_{NO}''}{Y_{NO}^{FPV''}}. \tag{42}$$

With this, Eq. (41) reduces to

$$\widetilde{\omega}_{NO} = \widetilde{\omega}_{NO}^{+} + \widetilde{Y}_{NO}\frac{\widetilde{\omega}_{NO}^{-}}{\widetilde{Y}_{NO}^{FPV}}. \tag{43}$$

The filtered source term contributions $\widetilde{\omega}_{NO}^{+}$, $\widetilde{\omega}_{NO}^{-}$, and $\widetilde{Y}_{NO}^{FPV}$ are precomputed by using the presumed PDF of Eq. (23) and are stored in a flamelet library $\widetilde{\mathcal{G}}_{\psi}^{e}$, which is parametrized in terms of $\widetilde{Z}$, $\widetilde{Z''^2}$, $\widetilde{C}$, and $\widetilde{H}$. In the following, transport equations are solved for these three mean quantities, and the residual scalar variance of the mixture fraction is obtained from an algebraic model.[31]
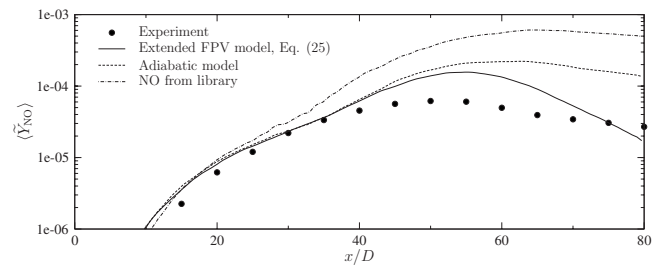

FIG. 16. Comparison of measured (symbols) and calculated (lines) mean NO mass fraction along the centerline for Sandia flame D.

A. Sandia flame D

The transport equation for the Favre-filtered NO mass fraction with the modeled source term, shown in Eq. (43), is solved in addition to the filtered scalar equations describing the evolution of mixture fraction, progress variable, and enthalpy, constituting the extended radiative FPV model. This model is applied in LES of Sandia flame D, and results for the NO formation are presented in the following. The effect of radiation on the NO formation for methane/air chemistry has been investigated in the context of the model analysis in Sec. III B. In that study, the effect of turbulence on the chemistry and radiation was not considered, and it was shown that the consideration of radiative heat losses reduced the NO formation by approximately 20%. In the present section, the effect of the interaction between turbulence, chemistry, and radiation is fully considered, and its dependence on the NO formation is quantified.

In Fig. 16, centerline profiles of the NO mass fraction from the simulations are compared to ensemble-averaged measurements. Additionally, results from the adiabatic simulation and $\widetilde{Y}_{NO}^{FPV}$ from the extended FPV library are shown. It can be seen that the predicted NO mass fraction from the adiabatic and radiative simulations are identical up to $x/D \approx 40$. This result is to be expected, since it was shown in Fig. 7 that both models predict a nearly identical temperature evolution in this region. The location of the peak NO formation is correctly predicted by the model; however, the peak NO value is overpredicted. It is interesting to point out that the adiabatic calculation considerably underpredicts the NO decrease in the fuel-lean part of the flame.

Mixture fraction-conditioned results at different axial locations in the jet flame are compared to experimental data in Fig. 17. It can be seen that the consideration of radiative heat losses results in a NO reduction by approximately 25–30%. The predictions from the radiative NO model are in good agreement with the unsteady flamelet model for the first three measurement stations. In conclusion, it is shown that the consideration of radiative effects is essential for the prediction of NO formation. It is demonstrated that the developed NO model yields considerably improved results compared to the steady flamelet model. NO predictions comparable with the unsteady flamelet model are obtained in the application of the model in the simulation of Sandia flame D. According to the results of the analysis presented in Sec. III B, NO predictions are expected to considerably improve for cases where thermal NO is dominant.
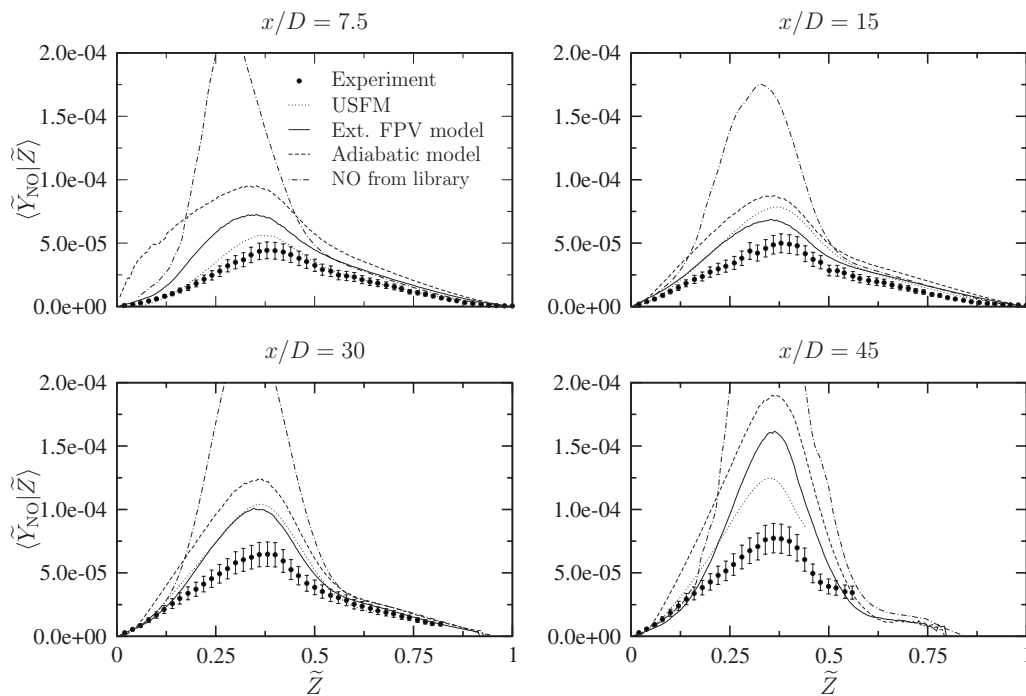
FIG. 17. Comparison of measured (symbols) and calculated (lines) conditional NO mass fractions at different streamwise locations in the flame. Experimental data are plotted with estimated uncertainties.

B. Pratt & Whitney combustor simulation

The model for the prediction of NO formation was applied in LES of the Sandia flame D experiment in the previous section. The experimental configuration of this flame consists of a central fuel nozzle, a pilot stream for flame stabilization, and a surrounding coflow. Despite the relatively simple geometrical setup, the turbulence/chemistry interaction in this configuration is sufficiently complex to serve as a validation case in the TNF workshop.[24] Results obtained for this free shear-flow configuration showed considerable improvements over previous model results for mean temperature and also mean NO mass fraction.

The successful validation against the Sandia flame experiment encouraged the application of the model to the Pratt & Whitney PW 6000 combustor configuration. The flow field inside the combustor is highly turbulent, swirling, and separated. The liquid fuel atomizes when entering the combustion chamber through the injector. In the combustion chamber, the droplets of fuel interact further by collision or coalescence until they eventually evaporate. The spray flame is stabilized by a recirculation zone, which is created by a swirling flow. Furthermore, air is injected into the combustion chamber through multiple jets, resulting in complex mixing patterns.

Compared with RANS-based models, LES has the potential to predict these unsteady, three-dimensional, geometry-dependent, coherent flow features, and their sensitivity to changes in the combustor design.[40,41] Therefore, numerical simulations of the combustor configuration are performed by using the unstructured, finite-volume LES solver CDP.[42,43] The code includes models for the droplet motion and the breakup and evaporation of the spray, and the gas phase chemistry is described by using the FPV model. The

different models for the liquid phase are summarized in the following for completeness. Further details can be found in Ref. 44 and references therein.

The droplet motion is modeled by using the Basset–Boussinesq–Oseen equations in the large density ratio limit between the droplet and gas phase. Under this assumption, the Basset force and the added mass term are small and are therefore neglected. The drag force on the droplet is modeled based on a solid particle with corrections accounting for particle deformation and internal circulation. The direct effect of the residual velocity on the droplet motion is neglected in the present model implementation. Moin and Apte,[44] however, pointed out that the particle motion is indirectly affected by the residual scales through the residual scale model that affects the resolved velocity field.

The atomization process is modeled by a residual secondary breakup model, which is based on a point particle approximation. The liquid fuel sheet, exiting the injector, is approximated by large drops with size equal to the size of the annulus. In the stochastic spray breakup model, it is assumed that the diameter of the droplet is a time-dependent stochastic variable with a given initial size distribution. The secondary breakup follows the temporal and spatial evolution of the distribution function obeying the Fokker–Planck equation. The breakup frequency and critical particle radius appearing in this equation are obtained from the balance between aerodynamic and surface tension forces.

The boundary layer surrounding the droplets are numerically not resolved, which would be necessary for the computation of the evaporation rates. Instead, the droplet evaporation rates are estimated from a uniform state model, and Lagrangian equations for the particle mass and heat transfer are solved. The individual source terms in these equations

TABLE I. Conditions for the Pratt & Whitney combustor configuration.

Parameter	Value
Stoichiometric condition ($-$)	$Z_{st}=0.0635$
Fuel stream ($-$, K)	$Y_{C_{10}H_{22}}=0.8256, Y_{C_9H_{12}}=0.1744, \Theta=171.4$
Oxidizer stream ($-$, K)	$Y_{O_2}=0.233, Y_{N_2}=0.767, \Theta=812$
Pressure (bar)	20.0

are modeled by using Spalding mass and heat transfer numbers and the Clausius–Clapeyron equilibrium vapor-pressure relationship.

The cooling effect of the gas phase due to the droplet evaporation is accounted for by computing an effective gaseous fuel temperature.[44] Therefore, the gaseous fuel temperature, which is used as a boundary condition in the solution of the flamelet equations, is reduced by the ratio of latent heat of evaporation divided by the specific heat capacity of the liquid fuel.

The combustor simulations are performed for take-off condition. The pressure in the combustion chamber at this operating condition is 20 bars. A surrogate fuel, consisting of 82.6% n-decane ($C_{10}H_{22}$) and 17.4% trimethylbenzene (C_9H_{12}) by mass is used as fuel. The chemical mechanism considers 113 species among 491 chemical reactions.[45] By using this mechanism with the boundary conditions given in Table I, flamelets are computed and compiled into a flamelet library. The simulations are performed for a 20° sector of the full combustor, which consists of a total of 18 injectors. The computational grid consists of 3.64×10^6 control volumes with a finer resolution in the region of the injector and the dilution holes. The Reynolds number, which is based on the nozzle diameter, air inlet velocity, and kinematic viscosity of air at inlet conditions, is approximately 725 000.

The Pratt & Whitney combustor is designed as a rich-quench-lean (RQL) combustor system, incorporating separate zones of combustion to maintain stability while reducing emissions. Combustion is initiated in the fuel-rich zone, in which all fuel is injected. The fuel partially reacts in an oxygen-lean environment and completes approximately 50% of the overall energy release. The combustion products in the fuel-rich zone consist mainly of CO and UHC and essentially no NO_x is formed.[46] The remaining air is rapidly injected in the quenching zone in order to reduce the combustion residence time near the stoichiometric condition. Past the quenching region, the reaction is then completed in the lean zone. In order to minimize NO_x emissions, it is essential to facilitate a rapid transition between the fuel-rich and fuel-lean zones to avoid long residence times around the stoichiometric condition.

In the following, the numerical results are discussed. Therefore, statistical data were collected over 250 nondimensional time units, corresponding to 50 ms real time or roughly 35 flow-through times, at which a flow-through time is defined from the length of the combustor and the characteristic inlet velocity. Note that the dilution holes are not shown in the figures, and all results are normalized.

Figure 18 shows instantaneous and averaged profiles of temperature and NO mole fraction along the axial plane through the combustor. The instantaneous droplet distribution is also shown in Fig. 18(a). The turbulent and complex flame structure and flow pattern can be observed in Figs. 18(a) and 18(b).

The instantaneous NO mole fraction is shown in Fig. 18(b). It can be seen that the NO formation in the primary zone is aligned with the surface of the stoichiometric mixture (shown by the solid line), which is determined by the spray angle. Some NO formation on the fuel-rich side of the flame

(a) Instantaneous Favre-filtered temperature (normalized)

(b) Instantaneous Favre-filtered NO mole fraction (normalized)

(c) Averaged temperature (normalized)

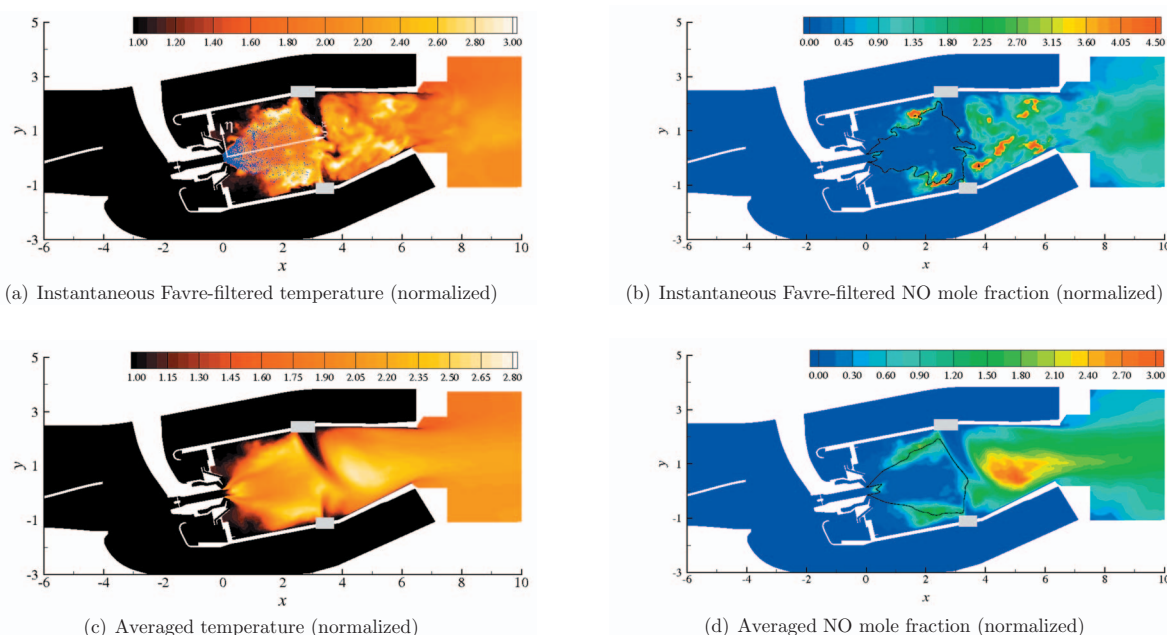(d) Averaged NO mole fraction (normalized)

FIG. 18. (Color) Contours of the instantaneous and mean temperatures and NO mole fractions along an axial cross section in a Pratt & Whitney aircraft engine combustor at take-off condition. The solid lines show the location of the stoichiometric mixture ($Z_{st}=0.0635$).

TABLE II. Comparison between experiment and simulation for averaged mean temperature and NO mole fraction at the combustor exit plane.

	$\langle\langle\widetilde{\Theta}\rangle\rangle/\langle\langle\Theta\rangle\rangle_{\mathrm{expt}}$	$\langle\langle\widetilde{X}_{\mathrm{NO}}\rangle\rangle/\langle\langle X_{\mathrm{NO}}\rangle\rangle_{\mathrm{expt}}$
Experiment	1	1
Extended FPV model, Eq. (25)	1.0437	1.3803
Adiabatic simulation	1.0393	4.2254

FIG. 20. Azimuthally averaged NO mole fraction profile at the combustor exit plane. Note that the dotted line corresponds to the spatially averaged NO mole fraction reported from the experiment and is only shown for visual reference.

is evident, suggesting that the prompt mechanism is most relevant for its formation. Figure 18(b) shows large regions with a high concentration of NO on the fuel-lean side, which is an indication of Zeldovich NO. Also, the finite residence time of the gas mixture when passing through the quench zone might be partially responsible for the NO formation.

Figures 18(c) and 18(d) show the averaged filtered temperature and NO contours. The NO formation rate is essentially zero in the droplet evaporation zone, which is due to the low temperature. The peak NO mole fraction in the primary zone is lower by a factor of 2 than in the secondary reaction zone. It is speculated that the large NO formation is mainly due to insufficient mixing intensity at the tip of the main cross-flow jet, resulting in longer residence times around the stoichiometric condition.

The mean temperature and mean NO mole fraction at the combustor exit are compared next. Circumferentially averaged quantities are denoted by $\langle\cdot\rangle$. Mean quantities, which are denoted by $\langle\langle\cdot\rangle\rangle$, are obtained from spatial averaging over the combustor exit plane.

The ratio between the mean temperature from the adiabatic simulation and the experimentally reported mean temperature is 1.0393. By accounting for radiation effects, this ratio increases to 1.0437. The slightly higher value of $\langle\langle\widetilde{\Theta}\rangle\rangle$ obtained from the radiative simulation is attributed to a shift in the location of the peak temperature. The comparison between experiments and simulation is summarized in Table II. The computed exit temperature profiles and the exit profile factor are compared to experimental data in Fig. 19. Whereas the radiative simulation predicts a peak in the temperature profile at the centerline of the combustor exit, the temperature maximum obtained from the adiabatic simulation is shifted toward the inner diameter. The profile factor, shown in Fig. 19(b), is in reasonable agreement with the measurements.
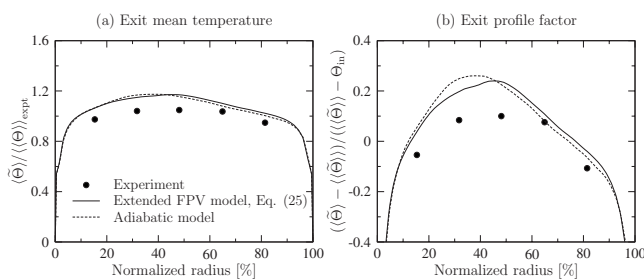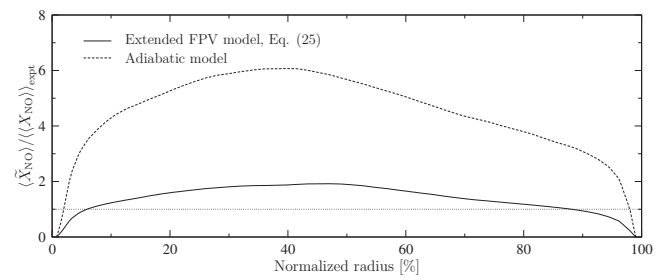
The circumferentially averaged NO mole fraction is shown in Fig. 20. For visual reference, the dotted line indicates the spatially averaged and normalized NO mole fraction from the experiment. It can be seen that the location of the peak NO mole fraction shows good correlation with the peak temperature in Fig. 19. The ratio between the NO mole fractions from the radiative simulation and the experiment is 1.3803. This corresponds to an overprediction of 38%. Note also that $\langle\widetilde{X}_{\mathrm{NO}}\rangle$ from the adiabatic simulation is larger by a factor of approximately 4 than that from the radiative simulation. A better understanding of the differences between adiabatic and radiative NO predictions is obtained by analyzing mixture fraction-conditioned results.

Figure 21 shows the mixture fraction-conditioned data of NO mole fraction and temperature as a function of the normalized injector coordinate ξ in the combustor. The horizontal dashed lines show the location of the stoichiometric mixture and the vertical arrows indicate the location of the main air dilution holes in the combustor.

It can be seen from Figs. 21(a) and 21(b) that the conditional temperature fields show strong similarity between adiabatic and radiative simulations. Note, however, that the radiative simulation predicts considerably less NO formation in the primary reaction zone [Figs. 21(c) and 21(d)]. The effect of the secondary air injection on the NO production is evident around $\xi\approx3.15$. In the region following the quench zone, the adiabatic model predicts rapid formation of NO on the fuel-lean side, which is presumably formed via the Zeldovich mechanism. This rapid formation is not evident in the radiative simulation. The reason for this discrepancy is that the radiative model accounts for a finite NO formation time via the additionally introduced enthalpy variable.

The PDF of the Favre-filtered mixture fraction as a function of the injector coordinate is shown in Fig. 22(a). The liquid fuel droplets evaporate and the gaseous fuel mixes with the air in the primary zone. It is interesting to point out that at the end of the primary zone, a region is formed with a large probability around the stoichiometric condition. The rapid mixing in the quenching section reduces the mean mixture fraction to values below Z_{st}. Following the quenching, mixing continues in the secondary zone, which results in an approximately homogeneous mixture at the combustor exit with little variation around $\langle\widetilde{Z}\rangle=0.0234$.
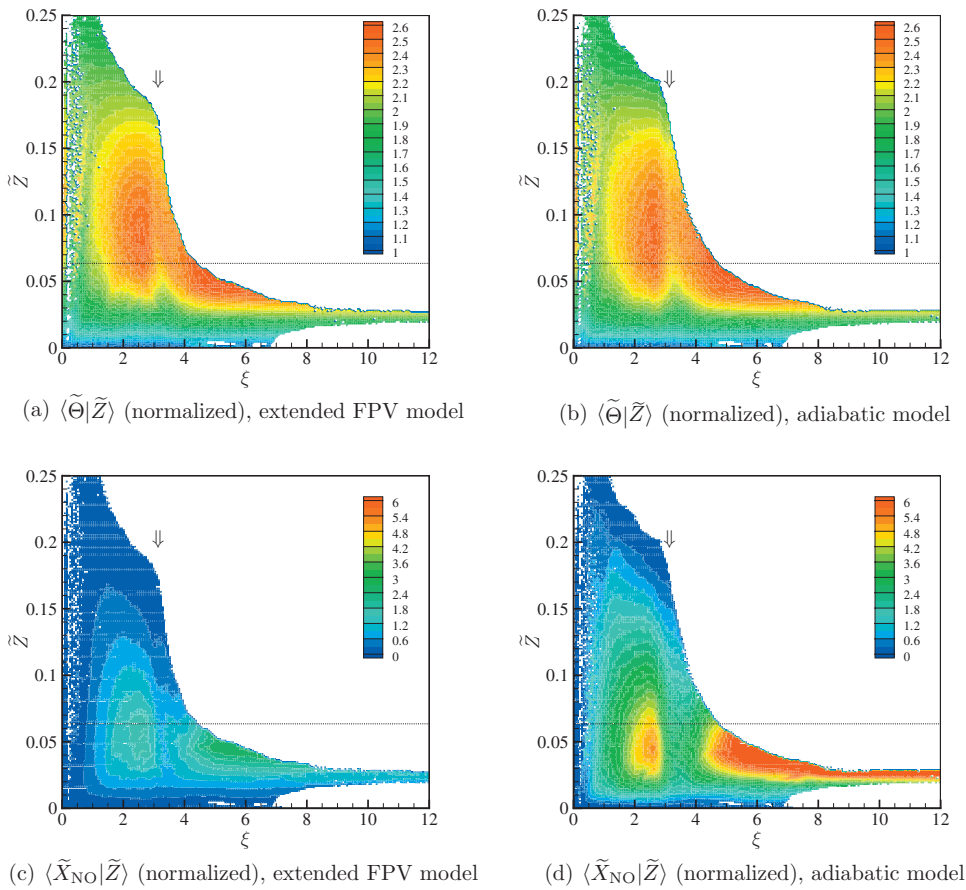

FIG. 19. Azimuthally averaged statistics at combustor exit plane: (a) normalized temperature and (b) temperature profile factor.

(a) $\langle \widetilde{\Theta} | \widetilde{Z} \rangle$ (normalized), extended FPV model

(b) $\langle \widetilde{\Theta} | \widetilde{Z} \rangle$ (normalized), adiabatic model

(c) $\langle \widetilde{X}_{\mathrm{NO}} | \widetilde{Z} \rangle$ (normalized), extended FPV model

(d) $\langle \widetilde{X}_{\mathrm{NO}} | \widetilde{Z} \rangle$ (normalized), adiabatic model

FIG. 21. (Color) Mixture fraction-conditioned data as a function of injector coordinate ξ [see Fig. 18(a)]; left column: simulation with radiation; right column: adiabatic simulation. The vertical arrows indicate the location of the dilution holes.

The probability of $\widetilde{Z} \leq Z_{\mathrm{st}}$ is used in the following as a metric to quantify the efficiency of the RQL system. The probability is given as

$$Q_{\mathrm{lean}}(\xi) = Q(Z_{\mathrm{st}}, \xi) = \int_0^{Z_{\mathrm{st}}} P(\widetilde{Z}; \xi) d\widetilde{Z}, \qquad (44)$$

which is computed from the LES, and is shown in Fig. 22(b). $Q_{\mathrm{lean}} = 1$ corresponds to the case where only lean mixture is present in a particular combustor section. Quantitative information of the RQL efficiency can be obtained by evaluating the steepest gradient of Q_{lean}, which occurs at the end of the dilution zone and the beginning of the secondary zone. In the limit of infinitely fast and complete mixing between the fuel-

rich mixture leaving the primary reaction zone and the dilution air, the gradient would approach infinity, corresponding to zero residence time around the stoichiometric condition. The stoichiometric mixing time can be estimated as

$$\tau_{\mathrm{RQL}} = (d_\xi Q_{\mathrm{lean}} u_{\mathrm{st}})_{\mathrm{max}}^{-1}. \qquad (45)$$

Evaluating τ_{RQL} for $\xi = 3.15$ with $d_\xi Q_{\mathrm{lean}} = 23.6$ m^{-1} and $u_{\mathrm{st}} = 27$ m/s from the simulation results in $\tau_{\mathrm{RQL}} = 1.57$ ms. Comparing this time scale with a characteristic Zeldovich NO formation time shows that the transition between fuel-rich and fuel-lean conditions is sufficiently fast in order to prevent thermal NO formation.

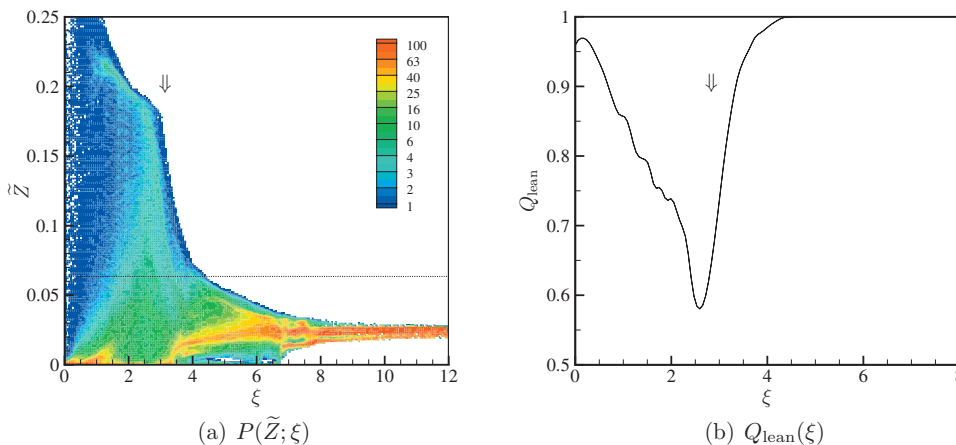(a) $P(\widetilde{Z}; \xi)$

(b) $Q_{\mathrm{lean}}(\xi)$

FIG. 22. (Color) PDF of Favre-filtered mixture fraction and probability of $\widetilde{Z} \leq Z_{\mathrm{st}}$ as a function of injector coordinate computed for a Pratt & Whitney aircraft engine combustor at take-off condition.

V. CONCLUSIONS

A model for the prediction of NO formation in turbulent nonpremixed flames was developed. The pronounced temperature sensitivity of the NO formation requires the accurate prediction of the flame temperature and the consideration of the interaction between turbulence and radiation. Therefore, in the first part of this paper, the flamelet/progress variable model was extended to account for radiative heat loss effects by introducing enthalpy as an additional variable. A transport equation for the enthalpy is solved and the radiative heat loss term is obtained from a flamelet library. However, since radiation occurs on relatively slow time scales, the radiative source term and all other thermochemical quantities are obtained from the unsteady flamelet solution in the composition space, in which radiation is of importance. The radiative FPV model was applied in LES of Sandia flame D, and the importance of the interaction between turbulence, radiation, and chemistry for the prediction of flame temperature and mixture fraction was discussed.

Based on the radiative FPV model, the second part of the paper addresses the prediction of nitric oxide formation. A consistent model formulation was developed. In this model, a transport equation for the NO mass fraction is solved, and the chemical source term is obtained from the flamelet library. Since the consumption rate contains information about the NO mass fraction, additional modeling is required. By employing a scale similarity argument, a closure model for the NO consumption rate is proposed. The NO model formulation is separately analyzed for three major NO formation mechanisms, namely, the thermal, nitrous oxide, and prompt NO pathways. Results obtained from this study show that the accuracy of the proposed model is comparable to the unsteady flamelet solution. Following this analysis, the model was applied in LES of Sandia flame D and a Pratt & Whitney aircraft engine combustor configuration. Mixture fraction-conditioned results for temperature and NO mole fraction in the aircraft combustor were compared between the adiabatic and radiative simulations. From the simulation, it was found that radiative effects have only a minor influence on the combustor exit temperature; however, it was found that consideration of heat losses is important for the accurate prediction of the nitric oxide formation.

APPENDIX: REACTION MECHANISM FOR NO FORMATION

The developed combustion model for the prediction of NO formation was validated in a separate model analysis in Sec. III B. Three different NO formation mechanisms were studied by reducing the GRI 2.11 mechanism[36] to only include
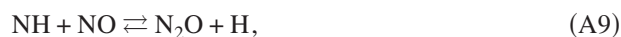

FIG. 23. Reaction flux diagram for Zeldovich mechanism of a partially premixed methane/air flame (Sandia flame experiment) at $\chi_{Z,st}=50$ s^{-1}.

the individual NO formation mechanisms: Zeldovich mechanism, N_2O mechanism, and prompt NO mechanism. These three mechanisms together with a reaction flux diagram, evaluated for a partially premixed methane/air flame at $\chi_{Z,st}=50$ s^{-1}, are summarized below. Note that the numeration of the individual reactions corresponds to that of the GRI 2.11 mechanism.

1. Zeldovich mechanism (see Fig. 23):

$$N + NO \rightleftarrows N_2 + O, \tag{A1}$$

$$N + O_2 \rightleftarrows NO + O, \tag{A2}$$

$$N + OH \rightleftarrows NO + H. \tag{A3}$$

2. Nitrous oxide mechanism (see Fig. 24):

$$N_2O + O \rightleftarrows N_2 + O_2, \tag{A4}$$

$$N_2O + O \rightleftarrows NO + NO, \tag{A5}$$

$$N_2O + H \rightleftarrows N_2 + OH, \tag{A6}$$

$$N_2O + OH \rightleftarrows N_2 + HO_2, \tag{A7}$$

$$N_2O + M \rightleftarrows N_2 + O + M, \tag{A8}$$

$$NH + NO \rightleftarrows N_2O + H, \tag{A9}$$

$$NCO + NO \rightleftarrows N_2O + CO. \tag{A10}$$

3. Prompt mechanism (see Fig. 25):

$$N + NO \rightleftarrows N_2 + O, \tag{A1}$$

$$N + O_2 \rightleftarrows NO + O, \tag{A2}$$

$$N + OH \rightleftarrows NO + H, \tag{A3}$$

$$NH + H \rightleftarrows N + H_2, \tag{A11}$$

$$NH_2 + H \rightleftarrows NH + H_2, \tag{A12}$$

$$CN + OH \rightleftarrows NCO + H, \tag{A13}$$

$$CN + O_2 \rightleftarrows NCO + O, \tag{A14}$$

FIG. 24. Reaction flux diagram for N_2O mechanism of a partially premixed methane/air flame (Sandia flame experiment) at $\chi_{Z,st}=50$ s^{-1}.
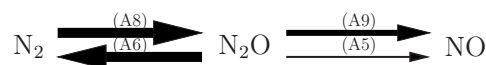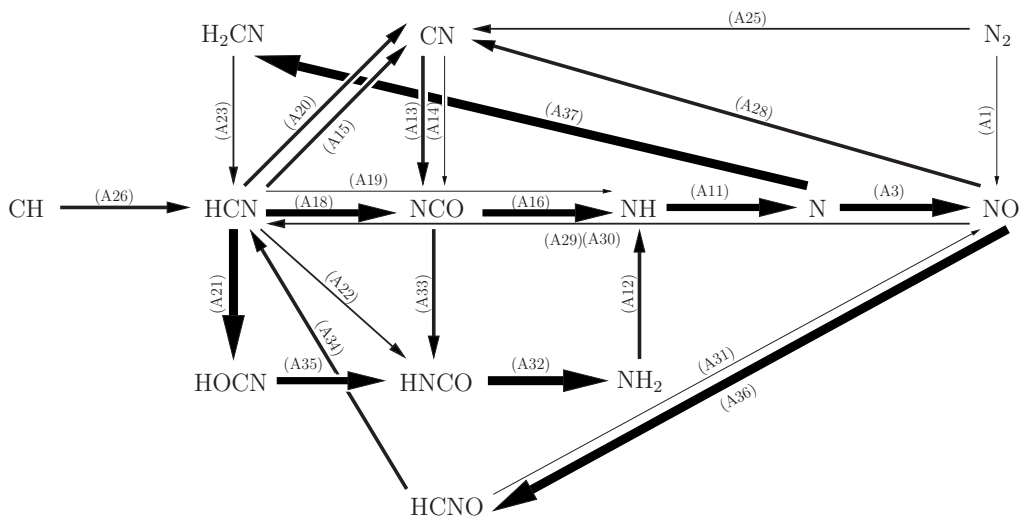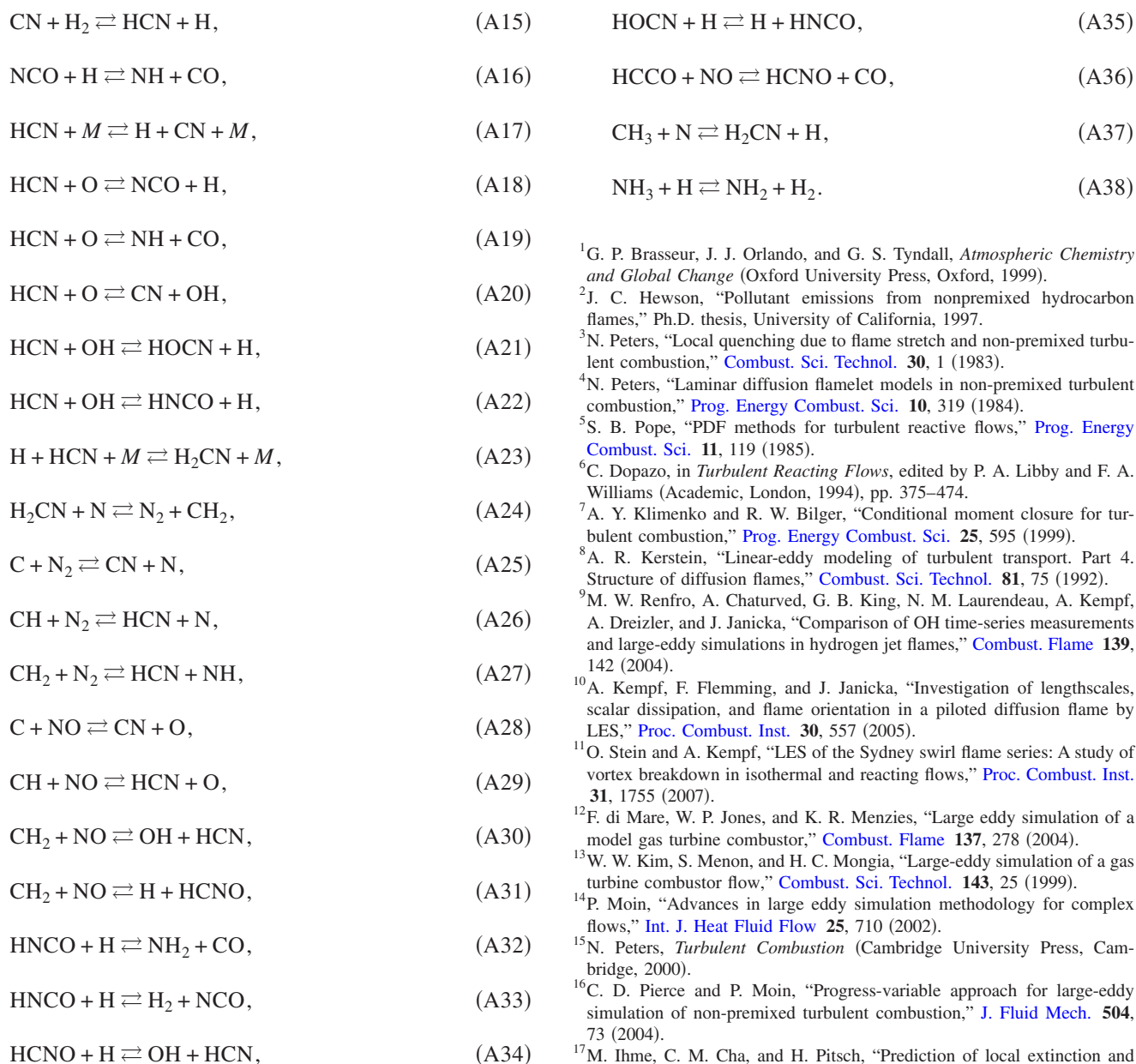
FIG. 25. Reaction flux diagram for prompt NO mechanism of a partially premixed methane/air flame (Sandia flame experiment) at $\chi_{Z,st}=50$ s^{-1}.

$$CN + H_2 \rightleftarrows HCN + H, \tag{A15}$$

$$NCO + H \rightleftarrows NH + CO, \tag{A16}$$

$$HCN + M \rightleftarrows H + CN + M, \tag{A17}$$

$$HCN + O \rightleftarrows NCO + H, \tag{A18}$$

$$HCN + O \rightleftarrows NH + CO, \tag{A19}$$

$$HCN + O \rightleftarrows CN + OH, \tag{A20}$$

$$HCN + OH \rightleftarrows HOCN + H, \tag{A21}$$

$$HCN + OH \rightleftarrows HNCO + H, \tag{A22}$$

$$H + HCN + M \rightleftarrows H_2CN + M, \tag{A23}$$

$$H_2CN + N \rightleftarrows N_2 + CH_2, \tag{A24}$$

$$C + N_2 \rightleftarrows CN + N, \tag{A25}$$

$$CH + N_2 \rightleftarrows HCN + N, \tag{A26}$$

$$CH_2 + N_2 \rightleftarrows HCN + NH, \tag{A27}$$

$$C + NO \rightleftarrows CN + O, \tag{A28}$$

$$CH + NO \rightleftarrows HCN + O, \tag{A29}$$

$$CH_2 + NO \rightleftarrows OH + HCN, \tag{A30}$$

$$CH_2 + NO \rightleftarrows H + HCNO, \tag{A31}$$

$$HNCO + H \rightleftarrows NH_2 + CO, \tag{A32}$$

$$HNCO + H \rightleftarrows H_2 + NCO, \tag{A33}$$

$$HCNO + H \rightleftarrows OH + HCN, \tag{A34}$$

$$HOCN + H \rightleftarrows H + HNCO, \tag{A35}$$

$$HCCO + NO \rightleftarrows HCNO + CO, \tag{A36}$$

$$CH_3 + N \rightleftarrows H_2CN + H, \tag{A37}$$

$$NH_3 + H \rightleftarrows NH_2 + H_2. \tag{A38}$$

[1] G. P. Brasseur, J. J. Orlando, and G. S. Tyndall, *Atmospheric Chemistry and Global Change* (Oxford University Press, Oxford, 1999).

[2] J. C. Hewson, "Pollutant emissions from nonpremixed hydrocarbon flames," Ph.D. thesis, University of California, 1997.

[3] N. Peters, "Local quenching due to flame stretch and non-premixed turbulent combustion," Combust. Sci. Technol. **30**, 1 (1983).

[4] N. Peters, "Laminar diffusion flamelet models in non-premixed turbulent combustion," Prog. Energy Combust. Sci. **10**, 319 (1984).

[5] S. B. Pope, "PDF methods for turbulent reactive flows," Prog. Energy Combust. Sci. **11**, 119 (1985).

[6] C. Dopazo, in *Turbulent Reacting Flows*, edited by P. A. Libby and F. A. Williams (Academic, London, 1994), pp. 375–474.

[7] A. Y. Klimenko and R. W. Bilger, "Conditional moment closure for turbulent combustion," Prog. Energy Combust. Sci. **25**, 595 (1999).

[8] A. R. Kerstein, "Linear-eddy modeling of turbulent transport. Part 4. Structure of diffusion flames," Combust. Sci. Technol. **81**, 75 (1992).

[9] M. W. Renfro, A. Chaturved, G. B. King, N. M. Laurendeau, A. Kempf, A. Dreizler, and J. Janicka, "Comparison of OH time-series measurements and large-eddy simulations in hydrogen jet flames," Combust. Flame **139**, 142 (2004).

[10] A. Kempf, F. Flemming, and J. Janicka, "Investigation of lengthscales, scalar dissipation, and flame orientation in a piloted diffusion flame by LES," Proc. Combust. Inst. **30**, 557 (2005).

[11] O. Stein and A. Kempf, "LES of the Sydney swirl flame series: A study of vortex breakdown in isothermal and reacting flows," Proc. Combust. Inst. **31**, 1755 (2007).

[12] F. di Mare, W. P. Jones, and K. R. Menzies, "Large eddy simulation of a model gas turbine combustor," Combust. Flame **137**, 278 (2004).

[13] W. W. Kim, S. Menon, and H. C. Mongia, "Large-eddy simulation of a gas turbine combustor flow," Combust. Sci. Technol. **143**, 25 (1999).

[14] P. Moin, "Advances in large eddy simulation methodology for complex flows," Int. J. Heat Fluid Flow **25**, 710 (2002).

[15] N. Peters, *Turbulent Combustion* (Cambridge University Press, Cambridge, 2000).

[16] C. D. Pierce and P. Moin, "Progress-variable approach for large-eddy simulation of non-premixed turbulent combustion," J. Fluid Mech. **504**, 73 (2004).

[17] M. Ihme, C. M. Cha, and H. Pitsch, "Prediction of local extinction and

re-ignition effects in non-premixed turbulent combustion using a flamelet/progress variable approach," Proc. Combust. Inst. **30**, 793 (2005).

[18]M. Ihme, "Pollutant formation and noise emission in turbulent non-premixed flames," Ph.D. thesis, Stanford University, 2007.

[19]P. J. Coelho and N. Peters, "Unsteady modelling of a piloted methane/air jet flame based on the Eulerian particle flamelet model," Combust. Flame **124**, 444 (2001).

[20]K. N. C. Bray and N. Peters, *Turbulent Reacting Flows*, edited by P. A. Libby and F. A. Williams (Academic, New York, 1994), pp. 63–113.

[21]B. Marracino and D. Lentini, "Radiation modelling in non-luminous non-premixed turbulent flames," Combust. Sci. Technol. **128**, 23 (1997).

[22]M. Hossain, J. C. Jones, and W. Malalasekera, "Modelling of a bluff-body nonpremixed flame using a coupled radiation/flamelet combustion model," Flow, Turbul. Combust. **67**, 217 (2001).

[23]H. Pitsch, M. Chen, and N. Peters, "Unsteady flamelet modeling of turbulent hydrogen-air diffusion flames," Proc. Combust. Inst. **27**, 1057 (1998).

[24]R. S. Barlow, web site for the International Workshop on Measurement and Computation of Turbulent Nonpremixed Flames (TNF) (http://www.ca.sandia.gov/TNF/), 1996.

[25]R. S. Barlow and J. H. Frank, "Effects of turbulence on species mass fractions in methane/air jet flames," Proc. Combust. Inst. **27**, 1087 (1998).

[26]V. R. Kuznetsov and V. A. Sabel'nikov, *Turbulence and Combustion*, (Hemisphere, New York, 1990).

[27]R. S. Barlow, A. N. Karpetis, J. H. Frank, and J.-Y. Chen, "Scalar profiles and NO formation in laminar opposed-flow partially premixed methane/air flames," Combust. Flame **127**, 2102 (2001).

[28]G. L. Hubbard and C. L. Tien, "Infrared mean absorption coefficients of luminous flames and smoke," Trans. ASME **100**, 234 (1978).

[29]J. H. Frank, R. S. Barlow, and C. Lundquist, "Radiation and nitric oxide formation in turbulent non-premixed jet flames," Proc. Combust. Inst. **28**, 477 (2000).

[30]P. J. Coelho, O. J. Teerling, and D. Roekaerts, "Spectral radiative effects and turbulence/radiation interaction in a non-luminous turbulent jet diffusion flame," Combust. Flame **133**, 75 (2003).

[31]C. D. Pierce and P. Moin, "A dynamic model for subgrid-scale variance and dissipation rate of a conserved scalar," Phys. Fluids **10**, 3041 (1998).

[32]R. S. Barlow, N. S. A. Smith, J.-Y. Chen, and R. W. Bilger, "Nitric oxide formation in dilute hydrogen jet flames: Isolation of the effects of radiation and turbulence-chemistry submodels," Combust. Flame **117**, 4 (1999).

[33]X. L. Zhu, J. P. Gore, A. N. Karpetis, and R. S. Barlow, "The effects of self-absorption of radiation on an opposed flow partially premixed flame," Combust. Flame **129**, 3425 (2002).

[34]H. Pitsch and H. Steiner, "Large-eddy simulation of a turbulent piloted methane/air diffusion flame (Sandia flame D)," Phys. Fluids **12**, 2541 (2000).

[35]H. Pitsch, "Improved pollutant predictions in large-eddy simulations of turbulent non-premixed combustion by considering scalar dissipation rate fluctuations," Proc. Combust. Inst. **29**, 1971 (2002).

[36]C. T. Bowman, R. K. Hanson, D. F. Davidson, W. C. Gardiner, V. Lissianski, G. P. Smith, D. M. Golden, M. Frenklach, and M. Goldenberg, GRI-MECH 2.11, 1997 (available from http://www.me.berkeley.edu/gri-mech/).

[37]Y. B. Zeldovich, "The oxidation of nitrogen in combustion explosions," Acta Physicochim. URSS **21**, 577 (1946).

[38]C. P. Fenimore, "Formation of nitric oxide in premixed hydrocarbon flames," Proc. Combust. Inst. **13**, 373 (1971).

[39]J. A. Miller and C. T. Bowman, "Mechanism and modeling of nitrogen chemistry in combustion," Prog. Energy Combust. Sci. **15**, 287 (1989).

[40]H. Mongia, *39th AIAA/ASME/SAE/ASEE Joint Propulsion Conference and Exhibit*, Huntsville, AL, 2003, Paper No. AIAA-2003-4495.

[41]W.-W. Kim and S. Syed, *42nd AIAA Aerospace Sciences Meeting and Exhibit*, Reno, Nevada, Paper No. AIAA-2004-331.

[42]K. Mahesh, G. Constantinescu, S. Apte, G. Iaccarino, F. Ham, and P. Moin, "Large-eddy simulation of reacting turbulent flows in complex geometries," Trans. ASME, J. Appl. Mech. **73**, 374 (2006).

[43]F. Ham, K. Mattsson, and G. Iaccarino, "Accurate and stable finite volume operators for unstructured flow solvers," Annual Research Briefs, Center for Turbulence Research, Stanford University/NASA Ames, 2006.

[44]P. Moin and S. V. Apte, "Large-eddy simulation of realistic gas turbine combustors," AIAA J. **44**, 698 (2006).

[45]N. Peters, personal communication (June 15, 2006).

[46]Pratt & Whitney and General Electric Aircraft Engines, "Critical propulsion components, Volume 2: Combustor," NASA/NASA Report No. CR-2005-213584/VOL2 2005.

[47]A. N. Karpetis and R. S. Barlow, "Measurement of flame orientation and scalar dissipation rate in turbulent partially premixed methane flames," Proc. Combust. Inst. **30**, 665 (2005).